





3D Traveling Ionospheric Disturbances During the 2022 Hunga Tonga–Hunga Ha’apai Eruption Using GNSS TEC

Mokhamad Nur Cahyadi^{1,2} , Buldan Muslim³, Ihsan Naufal Muafiry³, Aditya Riadi Gusman⁴ , Eko Yuli Handoko¹, Ira Mutiara Anjasmara¹ , Meilfan Eka Putra¹, Mega Wulansari¹, Dwi Sri Lestari¹, Shuanggen Jin^{5,6} , and Josaphat Tetuko Sri Sumantyo^{7,8}

Key Points:

- 3D ionospheric disturbances during the 2022 Tonga eruption was investigated with spatial and temporal direction
- The highest concentration of the electron disturbances was observed at an altitude of 200–300 km, which decreased at 500–600 km
- A correlation between ionospheric disturbances and the height of tsunami associated with eruption was observed

¹Department Geomatic Engineering, Institut Teknologi Sepuluh Nopember, Surabaya, Indonesia, ²Research Center for Science–Technology of Marine and Earth, Directorate of Research and Community Service, Institut Teknologi Sepuluh Nopember, Surabaya, Indonesia, ³Research Center for Climate and Atmosphere, National Research and Innovation Agency (BRIN), Bandung, Indonesia, ⁴GNS Science, Lower Hutt, New Zealand, ⁵Shanghai Astronomical Observatory, Chinese Academy of Sciences, Shanghai, China, ⁶School of Surveying and Land Information Engineering, Henan Polytechnic University, Jiaozuo, China, ⁷Center for Environmental Remote Sensing, Chiba University, Chiba, Japan, ⁸Department Electrical Engineering, Universitas Sebelas Maret, Surakarta, Indonesia

Supporting Information:

Supporting Information may be found in the online version of this article.

Correspondence to:

M. N. Cahyadi,
cahyadi@geodesy.its.ac.id

Citation:

Cahyadi, M. N., Muslim, B., Muafiry, I. N., Gusman, A. R., Handoko, E. Y., Anjasmara, I. M., et al. (2024). 3D traveling ionospheric disturbances during the 2022 Hunga Tonga–Hunga Ha’apai eruption using GNSS TEC. *Journal of Geophysical Research: Space Physics*, 129, e2023JA031806. <https://doi.org/10.1029/2023JA031806>

Received 22 JUN 2023

Accepted 26 JAN 2024

Author Contributions:

Conceptualization: Mokhamad Nur Cahyadi, Buldan Muslim, Ihsan Naufal Muafiry, Aditya Riadi Gusman

Data curation: Ira Mutiara Anjasmara, Shuanggen Jin

Formal analysis: Aditya Riadi Gusman, Eko Yuli Handoko, Meilfan Eka Putra, Mega Wulansari

Funding acquisition: Shuanggen Jin, Josaphat Tetuko Sri Sumantyo

Investigation: Eko Yuli Handoko, Ira Mutiara Anjasmara, Josaphat Tetuko Sri Sumantyo

Methodology: Mokhamad Nur Cahyadi, Buldan Muslim, Ihsan Naufal Muafiry, Aditya Riadi Gusman, Meilfan Eka Putra

Project administration: Shuanggen Jin, Josaphat Tetuko Sri Sumantyo

Resources: Eko Yuli Handoko, Shuanggen Jin

Software: Ihsan Naufal Muafiry

Supervision: Mokhamad Nur Cahyadi

Abstract The dual frequency Global Navigation Satellite System (GNSS) observations could determine the total electron content (TEC) in the ionosphere. In this study, GNSS TEC was applied to detect traveling ionospheric disturbances (TIDs) after the eruption of Hunga Tonga–Hunga Ha’apai (HTHH) on 15 January 2022. The eruption caused two types of tsunamis, first is tsunami generated by atmospheric wave (meteotsunami) and second is caused by eruption induces water displacement or tsunami classic. At the same time with former tsunami, the atmospheric wave (shock and lamb waves) also caused TIDs at a speed of approximately ~0.3 km/s. We found moderate correlation between this TIDs amplitude and the tsunami wave height model from tide gauge stations in New Zealand (0.64) and Australia (0.65). Further we attempted to reveal 3D structure of the TIDs in New Zealand, South Australia, and Philippines using 3D tomography. The tomography was set up > 1,170 blocks, as large as 1.0° (east–west) × 1.0° (north–south) × 100 km (vertical), up to 600 km altitude over selected regions. Tomogram shows beautiful concentric directivity of the first TIDs generated by atmospheric wave (AW).

1. Introduction

GNSS is a useful tool for monitoring and mitigating tsunami disasters in the fields of geodesy and geomatics. It has been used for accurate positioning on the Earth’s surface, as well as for monitoring water vapor in the atmosphere (Cahyadi et al., 2018) and land subsidence (Anjasmara et al., 2018). Furthermore, GNSS satellite observations were used to determine the TEC in the ionosphere layer (Jin et al., 2022), which is in the form of electron density along the line of sight (LoS) known as the slant TEC (STEC) and in the vertical form known as the vertical TEC (VTEC). The ionosphere layer can be disrupted by earthquakes, tsunamis, volcanic eruptions, and other natural disasters, and these anomalies have been observed using the GNSS TEC. During these events, acoustic waves propagate upward to the ionosphere layer and are monitored using the TEC (Cahyadi, 2014; Cahyadi et al., 2018, 2022; Cahyadi & Heki, 2013a, 2013b, 2015; Heki & Cahyadi, 2012; Jin et al., 2015; Jin & Su, 2019; Liu et al., 2011; Sharma et al., 2017), tsunamis (Kakinami et al., 2012; Liu et al., 2006; Muslim et al., 2020; Rolland et al., 2010), geomagnetic storms (Jenan et al., 2022; Jin et al., 2017; Sori et al., 2021), and volcanic eruption (Cahyadi et al., 2020, 2021; Nakashima et al., 2014, 2016; Shults et al., 2016). This is due to the fact that these natural disasters are propagating acoustic waves upward to the ionosphere layer, which was monitored using the TEC (Cahyadi & Heki, 2015).

HTHH experienced a strong eruption with a volcanic explosivity index (VEI) of 5 at around 04:15 UT on 15 January 2022, in the South Pacific Ocean (Heki, 2022). At around 06:00 UT, the atmospheric barometer station in New Zealand detected an atmospheric wave as a positive pressure spike (Figure S3 in Supporting Information S1). The same was observed by Weathernews (2022), which detected atmospheric waves from the southeast to the northwest as a positive pressure spike of several hectopascals around 7 hr after the HTHH eruption using a series of atmospheric barometers in Japan, which is about 8,000 km from HTHH. The positive pressure spike indicates a change in air pressure due to heat energy from the HTHH eruption. The presence of a surge wave of positive pressure in the atmosphere is induced by a Lamb wave (LW) (Heki, 2022; Kanamori et al., 1994). A LW

Validation: Buldan Muslim, Ira Mutiara Anjasmara, Meilfan Eka Putra, Dwi Sri Lestari, Josaphat Tetuko Sri Sumantyo

Visualization: Aditya Riadi Gusman, Eko Yuli Handoko, Ira Mutiara Anjasmara, Meilfan Eka Putra, Mega Wulansari, Dwi Sri Lestari

Writing – original draft: Mokhammad Nur Cahyadi, Buldan Muslim, Ihsan Naufal Muafiry, Aditya Riadi Gusman, Meilfan Eka Putra, Mega Wulansari, Dwi Sri Lestari

Writing – review & editing: Mokhammad Nur Cahyadi, Buldan Muslim, Ihsan Naufal Muafiry, Mega Wulansari, Dwi Sri Lestari

is a type of wave that propagates on the Earth's surface at a speed of sound (~ 0.3 km/s) (Kanamori et al., 1994). Increases in pressure and temperature can cause a slow wave to travel from the troposphere to the ionosphere. This is supported by a study conducted by Ogawa et al. (1982), who analyzed ionospheric disturbances caused by the eruption of St. Helens with a VEI of 5 over the northwestern United States in 1980. They concluded that the disturbance was caused by a long-wave motion. LW from volcanoes generate energy that leaks from the troposphere into the ionosphere, producing signals in the ionosphere.

Several studies have elucidated TIDs caused by HTHH eruption, including those conducted by Heki (2022), Themens et al. (2022), Aa et al. (2022), Zhang, Vierinen, et al. (2022), Astafyeva et al. (2022), Saito (2022), Harding et al. (2022), and Muafiry et al. (2022). Themens et al. (2022) found that two distinct large-scale TIDs radially propagated outward from the Tonga eruption site, along with several subsequent medium-scale TIDs. TIDs were tracked using more than 4,735 globally distributed GNSS stations. Saito (2022) also analyzed TIDs observed over Japan using a GNSS receiver network and identified two types of TIDs exhibiting different characteristics. However, all previous studies used GNSS TEC data to analyze ionospheric disturbances during the tsunami caused by the HTHH eruption in 2D manner. These studies focused only on one area of GNSS observation, but none evaluated the 3D spatial and temporal distributions of these ionospheric disturbances. Tomography is a tool to observe ionospheric disturbances caused by the eruption of HTHH in 2022 using GNSS TEC. This involves applying the ionospheric linear combination method to determine the TEC values used to generate a 3D model through tomography. Cahyadi et al. (2022a, 2022b), Muafiry et al. (2018), and Muafiry and Heki (2020) observed that this method successfully calculated ionospheric disturbance models. Thus, these previous studies showed that the 3D tomography method can provide a spatial picture of ionospheric disturbances.

The eruption was detected by various Deep-ocean Assessments and Reporting of Tsunamis (DART) and tidal stations in surrounding countries such as Australia, New Zealand, and the Philippines. Omira et al. (2022) conducted a comparative study of the travel times of tsunamis recorded at the sea surface and those induced by moving acoustic-gravity waves using tsunami elevation modeling. They also compared the global distributions of the maximum simulated tsunami wave amplitudes to those observed at offshore observatories (DART buoys). While some correlations were found between tsunami arrival times and Acoustic Gravity Waves (AGWs), none of the previous studies above addressed the height of the tsunami amplitude or the magnitude of TIDs. In this research, several updates to complement existing research emerged: (a) We visualized the model of TIDs spatially and temporally using the 3D tomography method using GNSS TEC. (b) We further analyzed the relationship between TIDs and tsunami height. (c) The effects of shock waves (SW) and LW up to ~ 500 km altitude were observed using 3D tomography; these findings concur with data obtained from radio occultation methods, where TIDs can reach up to ~ 500 km altitude (Shinagawa & Miyoshi, 2023). (d) Ionospheric disturbances resulting from HTHH eruptions in areas near the HTHH, especially in Australia and New Zealand, were examined using the previous research. Moreover, we analyzed the TIDs in the Philippines.

2. Data and Methods

2.1. Hunga–Tonga Explosion and Model of Tsunami

HTHH, an uninhabited volcanic island in the southwest Pacific Ocean located on the coordinates 20.57°S and 175.38°W erupted with a VEI of 5–6 on 15 January 2022, after an increase in volcanic activity in December 2021 (Heidarzadeh, et al., 2022). It was recorded as one of the biggest explosions in the last 30 years (Omira et al., 2022; Witze, 2022). The onset and expansion of explosion and cloud were observed by Omira et al. (2022) from 04.00 to 05.20 UTC using an optical medium on the GOES-17 satellite imagery. Further analyzed in this study using the Himawari 8 satellite from the Center for Environmental Remote Sensing at Chiba University (Takenaka et al., 2020; Yamamoto et al., 2020). This was conducted at 10 min intervals from 13:20 to 15:30 JST (04:30–06:30 UTC) as presented in Figure S1. The explosion had an atmospheric acoustic gravitational wave pattern that spread concentrically and propagated from the sea level to the ionosphere and later traveled radially outward several times (Andrews, 2022; Duncombe, 2022; Omira et al., 2022).

The HTHH eruption led to the discovery of tsunamis that were sent along the Pacific coast, including Tonga, Fiji, American Samoa, and Vanuatu, and the waves reached New Zealand, Japan, the United States, Chile, and Peru (Vergoz et al., 2022). The DART system was specifically designed to measure tsunamis in the deep ocean (Eble & Gonzalez, 1991; Meinig et al., 2005) by recording pressure changes resulting from both atmospheric conditions

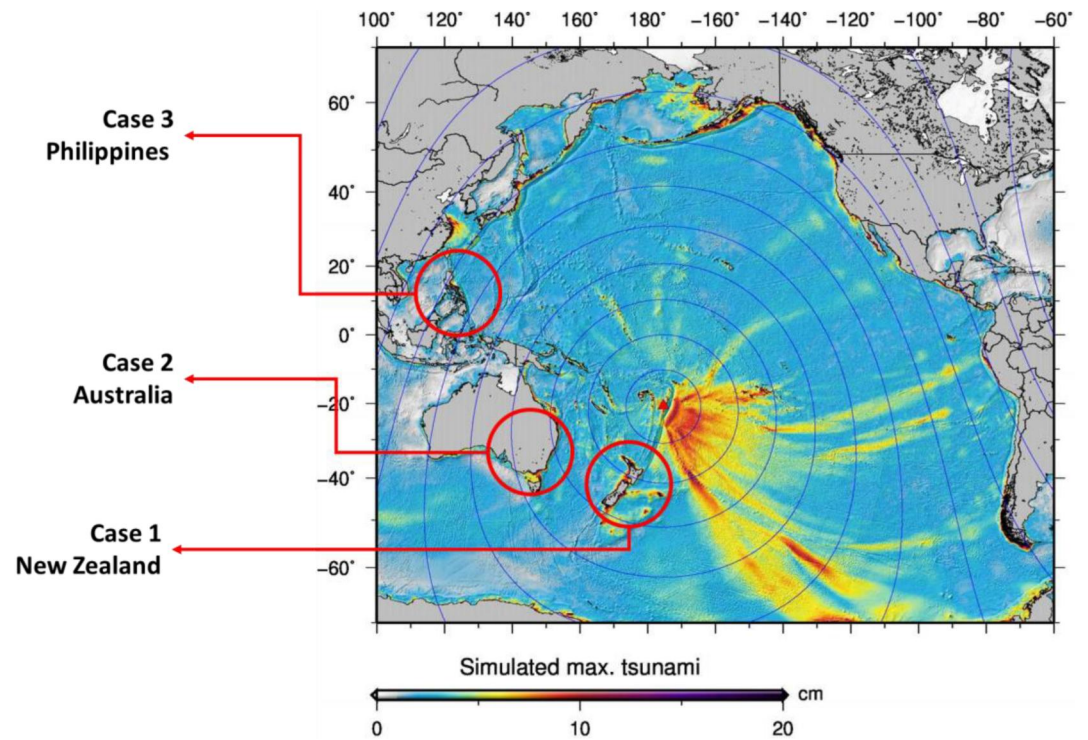


Figure 1. Simulated maximum tsunami amplitude from the air-wave tsunami source model of 2022 Hunga Tonga–Hunga Haʻapai volcanic tsunami (Gusman et al., 2022). The blue contours show the travel time of the air wave from the HTHH volcano (red triangle) with a 1-hr interval whereas the red circle indicates the observed area.

and the movement of water waves (Gusman et al., 2022). In the study, by Gusman and Roger (2022), they conducted a tsunami simulation using a circular sea-surface deformation model with a 10-km diameter, as presented in Figure 1. The simulation was supported by direct measurement data obtained from DART, and from the state-owned tidal station closest to the location of the HTHH eruption. The study focused on the regions closest to the eruption source, namely, eastern Australia, New Zealand, and the Philippines. GNSS observation stations were also utilized to detect any ionospheric disturbances, and their proximity to the study areas was considered.

2.2. GNSS Data

The data used were obtained from the Australian Regional GNSS Network station in Australia and GeoNet in New Zealand with a 30-s observation interval of 30. The Philippine Active Geodetic Network (PAGEtNet) data with a 1-s observation interval was also used. Furthermore, the Receiver Independent Exchange data format was converted from PAGEtNet into 30-s intervals to have the same gaps as those in other study areas and also to reduce the size. The locations of the GNSS stations in New Zealand, Australia, and the Philippines are presented in Figure 2. Under the geomagnetic latitudinal conditions, each center of the tomography model in the region is at different angles of geomagnetic field inclination, as presented in Table 1.

2.3. TEC Estimation

GPS and GLONASS propagate electromagnetic signals through the ionosphere before being received by the receivers on Earth. The GPS phase difference between L1 (~1.5 GHz) and L2 (~1.2 GHz) has been changed to STEC. On the other hand, the GLONASS phase difference between G1 (~1.6 GHz) and G2 (~1.3 GHz) has been converted to STEC. The STEC represents the electron-density value along the LoS. In this study, VTEC was calculated from STEC in a short time variation and subtracted from its polynomial. Furthermore, the electron-density values were expressed in TECU (1 TECU = 10^{16} electrons/m²). The point at 300 km the ionosphere intersects the LoS layer was referred to as the ionospheric penetration point, whereas the projection on the surface was known as the sub-ionospheric point (SIP).

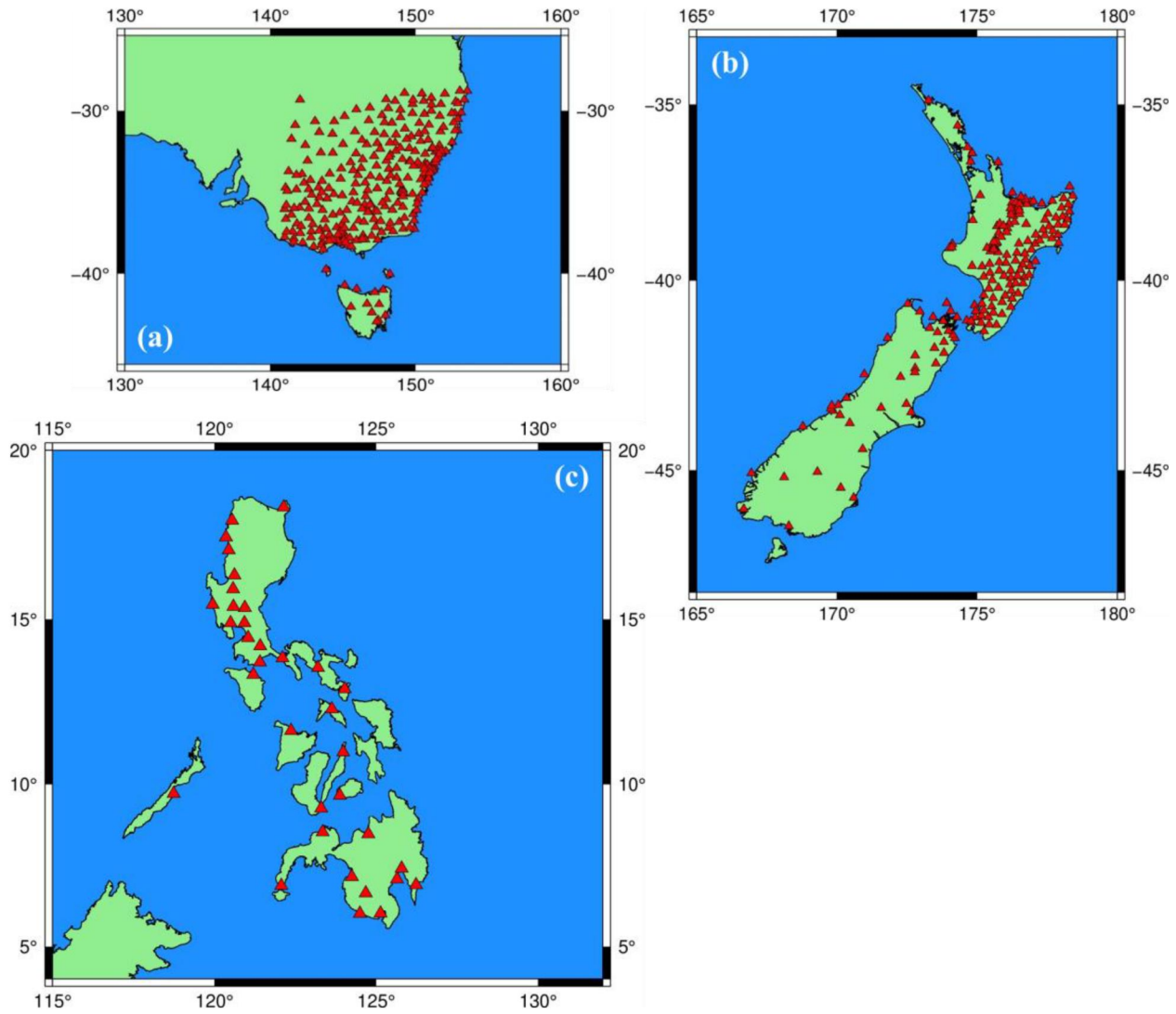


Figure 2. Locations of the GNSS observation stations in Australia (a), New Zealand (b), and the Philippines (c). Red triangles indicate the location of the stations; green areas, the land; and blue areas, the sea.

In this study, we used STEC that calculated from the phase difference of the two frequencies was determined by calculating the L1 and L2 by eliminating ambiguity, cycle slip, and bias frequency in the phase data (Abidin, 2000). Multiplication of the L4 value by the scale factor produced TEC value as indicated in the following Equations 1 and 2:

$$\Delta L_4 = L_1 - L_2 \quad (1)$$

$$STEC = \frac{1}{40.308} \times \frac{f_1^2 \times f_2^2}{(f_1^2 - f_2^2) \Delta L_4} \quad (2)$$

where f_1 and f_2 denote the frequencies of the L1 and L2 signals (~1.2 and ~1.5 GHz). The 40,308 coefficient was used to convert ionospheric delay value to TEC (Muafiry & Heki, 2020), whereas the ionospheric signature of TIDs was modeled using differential TEC (dTEC). Notably, the dTEC was developed using the best-fitting method with a high degree. This method has

Table 1

Geographic and Magnetic Coordinate Based on

Region	Center long (°)	Center lat (°)	MLat/Inc (°)
New Zealand	176	-40	-65.199
Australia	149	-34	-64.843
Philippines	125	12.5	12.131

Source: Magnetic inclination was calculated using the World Magnetic Model 2020 Calculator.

the ability to eliminate noise caused by the movement of the satellite. Meanwhile, orbiting and TEC fluctuation values were determined using irregular up and down graphs (Heki, 2011).

2.4. 3D Tomography

Tomography is a cross-sectional imaging of an object from either transmission or reflection data collected by illuminating the object from different directions. TEC has been utilized in ionosphere studies to reconstruct the state of the ionosphere using satellite data by monitoring electron-density distribution represented by the TEC along the LoS. It is noteworthy that block tomography was assumed to be homogeneous (Muafiry, et al., 2018). The size resolution of the tomography model in each 100-km altitude layer was set to have the same dimensions, which were 1° east–west and 1° north–south, as presented in Figure S2. The division of ionospheric values by LoS produced electron-density values within each fault block based on the LoS penetration depth. Furthermore, the length of the two LoS intersections was calculated with the sides of the fault block to determine the penetration depth. The density value of the fault block was also determined using the following equation (He & Heki, 2018):

$$\Delta STEC = \sum_{j=1}^n A_{ij} x_j + e_i \quad (3)$$

Equation (3) was used to collect the density values for every fault block that the LoS crossed based on the complete dTEC density value and extended component of the LoS penetration for each block. The equation also incorporated the measurement error value of 0.05, with TECU assumed as a result of the usual error in differential GNSS metering (Coster et al., 2013).

3. TIDs and Propagation

3.1. TIDs

The STEC was calculated using a linear combination of the ionosphere along the LoS from the satellite to the receiver. Furthermore, the comparison and TEC values were merged using a polynomial reference curve such that the polynomial was formulated in the “order 10” based on the line of best fit. The ionospheric disturbances were detected through the residual STEC values that were significantly different from the reference curve. In addition, the TEC change was calculated and the TEC value with a 10th-degree polynomial subtracted to obtain the outliers so as to determine the dTEC. Notably, the significant changes in the dTEC associated with the ionosphere density were detected in New Zealand before the arrival time of the tsunami by GPS PRN 10, 18, 23, 24, and 32 and GLONASS 47; those in Australia by GPS PRN 10, 21, and 32; and those in the Philippines by GPS PRN 8, 16, 21, and 26.

The TIDs in the time-series values for New Zealand were detected in six satellites, namely, GPS PRN 10, 18, 23, 24, and 32 and GLONASS 47, as presented in Figure 3. It is noteworthy that some satellites crossed over New Zealand territory as the tsunami waves propagated. The average TIDs were detected at a peak of 06:06–06:42 UT or approximately 114 min after eruption with ~2.3–3.4 TECU. This is consistent with the finding by Zhang, Vierinen, et al. (2022) and Aa et al. (2022) that the amplitude of the dTEC magnitudes was up to 3 TECU. TEC data observations show that in the New Zealand region there are several TIDs peaks at 06:00 UT and 08:00 UT (Figure 3). First, at ~06:00 UT, clearly visible TIDs was detected in New Zealand, characterized by fluctuations lasting ~40–60 min. It was reported that TIDs was caused by AW, specifically SW and LW. This inference was supported by the simultaneous increase in barometric air pressure, as shown in Figure S3b in Supporting Information S1. At ~06:00 UT, AW phenomenon also occurred, leading to the manifestation of global meteo-tsunami. The phenomenon is also in line with Gusman et al. (2022), which reported tsunami detected at the same hour in New Zealand. The timeline of events is shown in Figure S3a in Supporting Information S1, where AW precedes the detection of TIDs in the ionosphere, eventually followed by tsunami recording at the DART NZE station. Therefore, TIDs and tsunami detected at ~06.00 UT in New Zealand share a connection (not a causal relationship), as AW causes both phenomena. We discuss these atmospheric waves in more detail in the next sub-chapter regarding propagation speed and frequency.

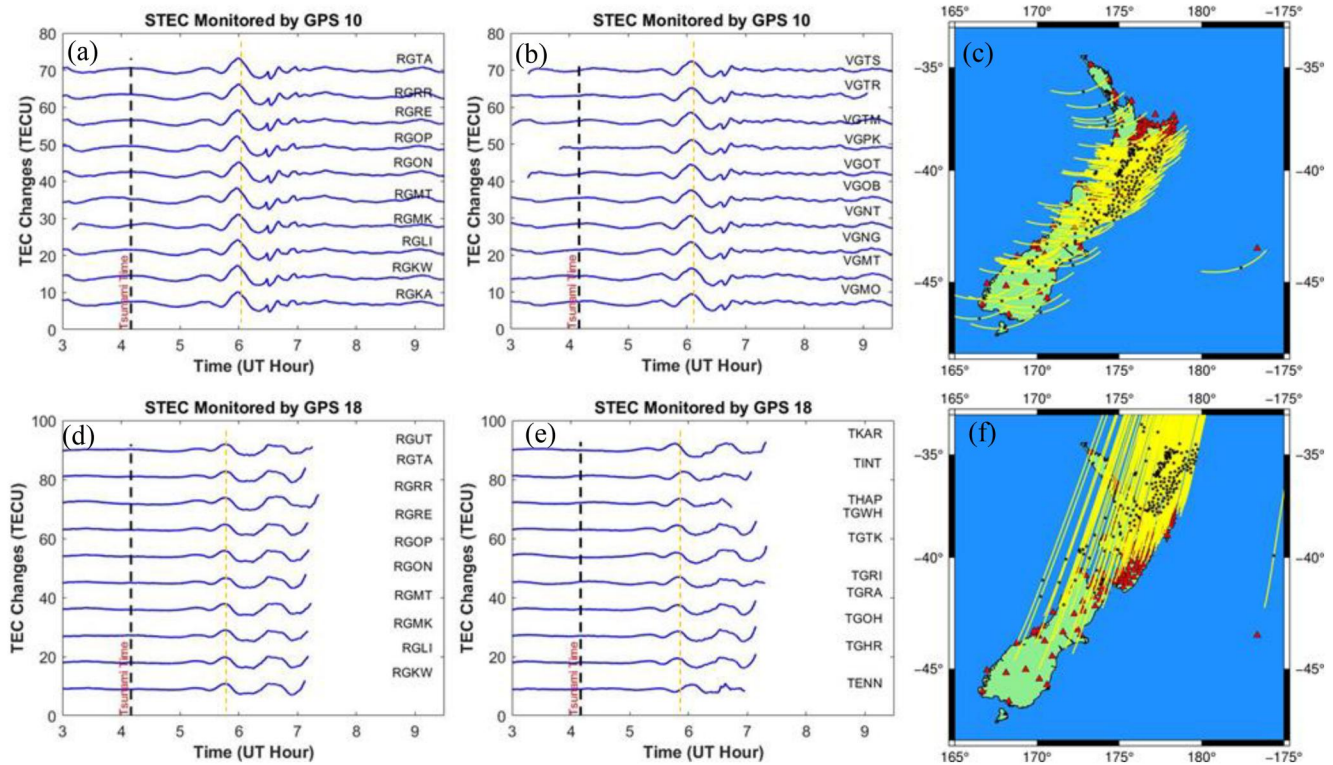


Figure 3. Time series of TEC residuals (a,b,d,e,g,h,j,k,m,n,p,q) and SIP trajectories (c,f,l,o,r) for New Zealand. The black dashed lines in the time series indicate the timing of eruption; red triangles, the spot of stations; yellow dashed lines in the time series, the peaks of the two TIDs; yellow lines, the trajectory of SIP at 06:30–08:30 UT; and black dots, the SIP when the TIDs were detected.

Examining the phenomenon at ~08:00 UT, Gusman et al. (2022) and Hu et al. (2023) reported that tsunami was recorded in New Zealand during this timeframe. It was presumed to be classical tsunami caused by eruption-induced water displacement, as seen in Figure 1c. TIDs detected at ~08.00 UT had a causal relationship with tsunami, originating from Gravity Wave (GW) propagating upward to the ionosphere. The second TIDs peak (Figure 3) occurred almost simultaneously with the sea level rise observed by Gusman et al. (2022), as shown in Figure S3b in Supporting Information S1. We suspect that these TIDs are caused by Internal Gravity Wave (IGW) caused by classical tsunamis. Furthermore, we try to determine the propagation speed of TIDs in sub-section 3.2. TIDs detected at ~08.00 UT had a causal relationship with tsunami, originating from IGW propagating upward to the ionosphere.

The directivity of TIDs was also analyzed, as presented in Figure S4 in Supporting Information S1. This represents the position of the SIP point in New Zealand from 05:48 to 06:18 UT accompanied by the TEC value observed. The positive dTEC was found to be moving southward due to the movement of the tsunami toward the direction, as previously stated by Zhang, Vierinen, et al. (2022). The TIDs area can be observed when there are more data on the number of detecting satellites and existing observation stations.

In the case of Australia, three satellites showed the presence of TIDs, as indicated in Figure 4. It was found that GPS PRN 10 and 32 observed TIDs with SIP in the coastal area whereas GPS PRN 21 observed the same in the inland area. The peak for the average TIDs was detected at 07:33–08:16 UT or approximately 114 min after eruption, with ~1.5–2.9 TECU. This is consistent with the findings of Aa et al. (2022) using GNSS data at stations spread across the country that the dTEC SIP value around Australia was ~2 TECU.

The TIDs areas detected by GPS satellites 10, 21, and 32 are presented in Figure S5 in Supporting Information S1, and these consist of the positions of SIP points from 07:06 to 07:54 UT as well as the dTEC values. Moreover, the movement directions of TIDs were found to be the same from both stations in Australia and New Zealand.

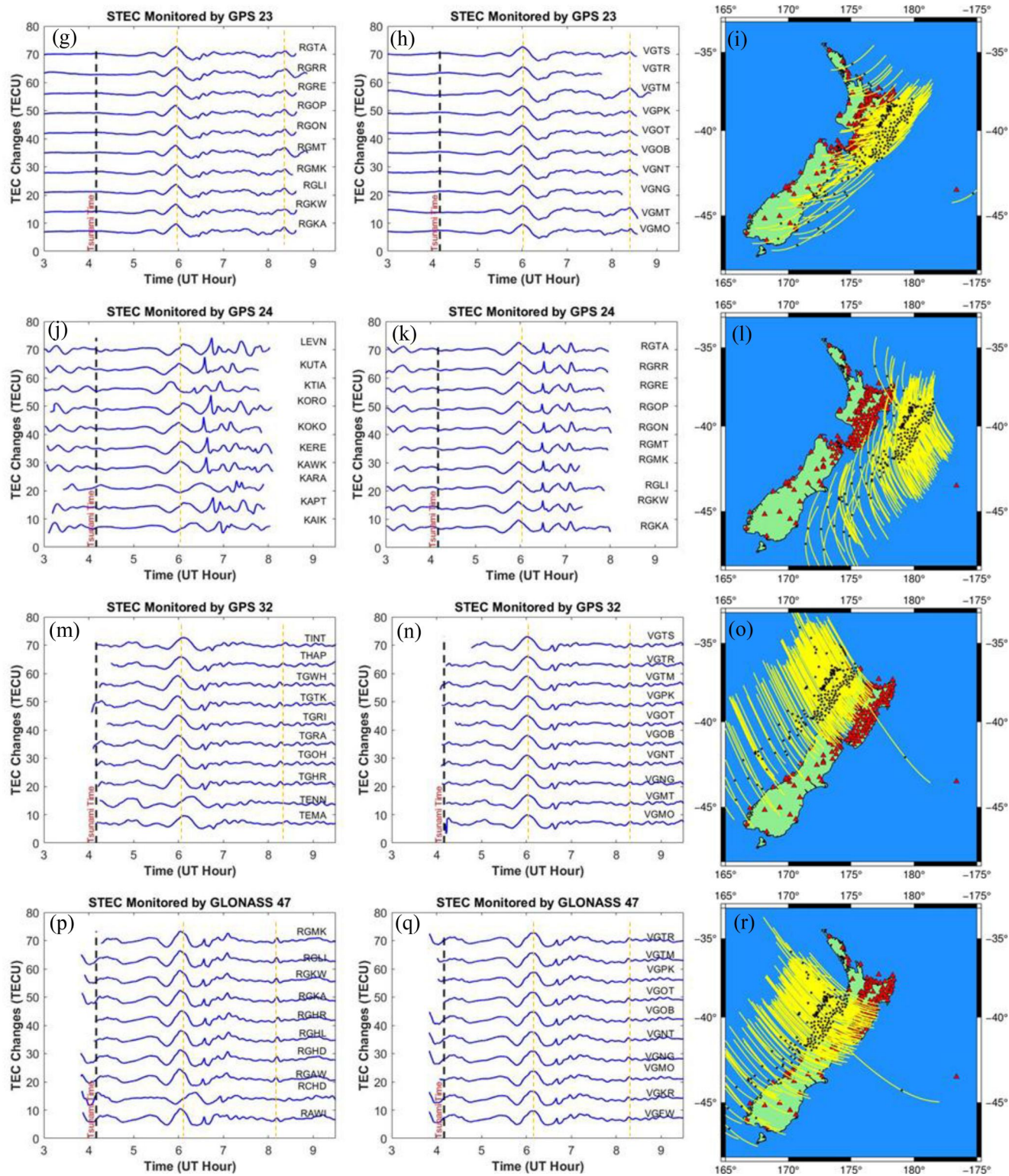


Figure 3. (Continued)

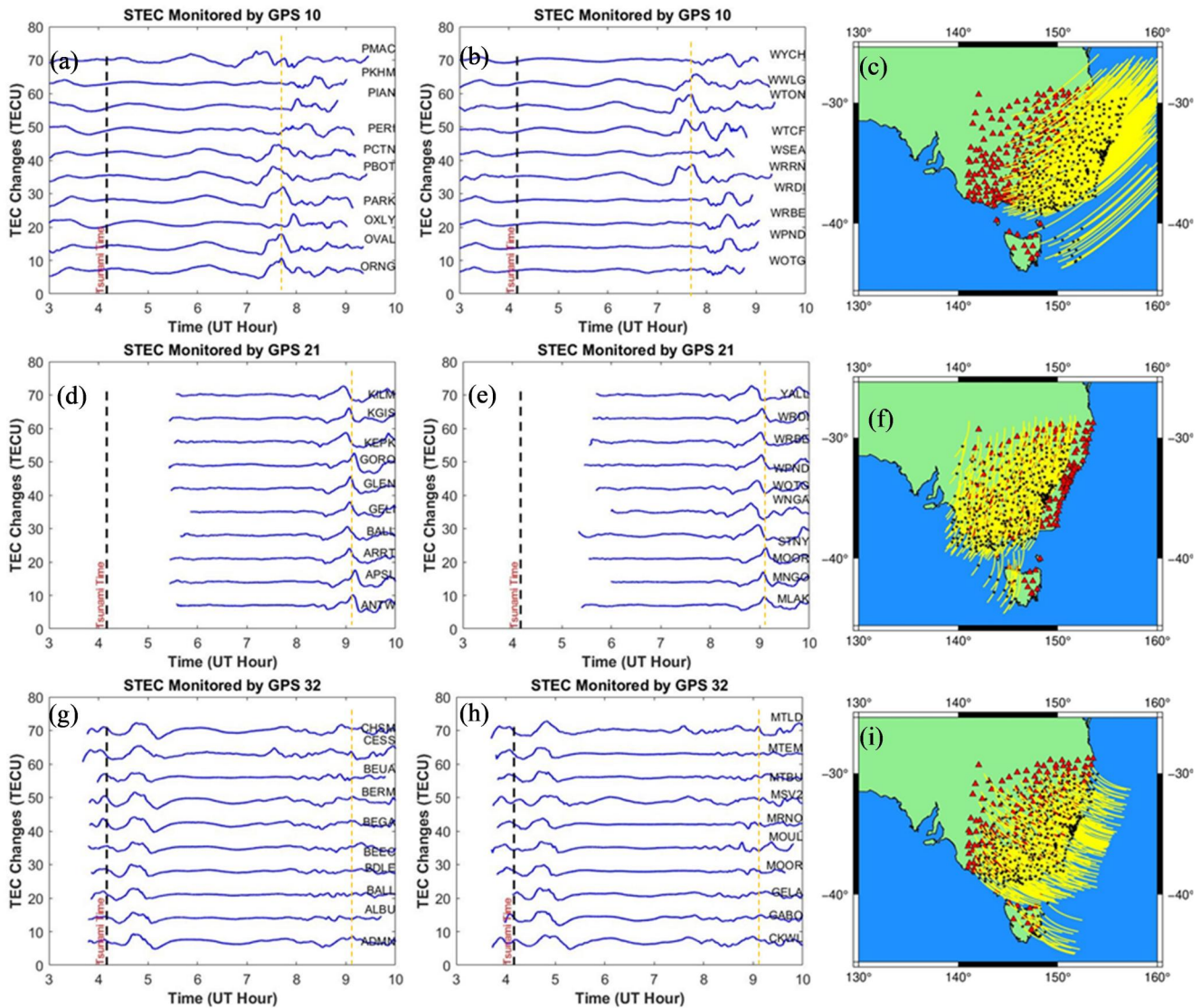


Figure 4. Time series of TEC residual (a,b,d,e,g,h) and SIP trajectory (c,f,i) in Australia. The black dashed lines in the time series indicate the timing of eruption; red triangles, the location of stations; yellow dashed lines in the time series, the peak of TIDs; yellow line, the trajectory of SIP at 06:30–08:30 UT; and black dots, the SIP when TIDs were detected.

Positive $dTEC$ was observed to have moved from the northeast to the southwest at around 07:06 UT and started disappearing at 07:54 UT.

In the case of the Philippines, TIDs were obtained from four satellites, including GPS PRN 8, 16, 21, and 26, as presented in Figure 5. The time series for the slant changes of TEC in the Philippines tended to fluctuate more than those for Australia and New Zealand, as presented in Figure 5. In addition, during the eruption, a moderate geomagnetic storm was detected with a Dst index value of up to -90 nT, as presented in Figure S6 in Supporting Information S1. The HTHH volcanic eruption occurred during the recovery phase of a moderate geomagnetic storm. Previous studies (Aa et al., 2022; Astafyeva et al., 2022; Li et al., 2023) stated that this geomagnetic storm had minimal impact on TEC. It was found that the peak of the average TIDs was at $\sim 09:00$ – $10:00$ UT or ~ 300 min after eruption with ~ 24.8 TECU. This is because the TIDs in the area were detected in the afternoon, local time, causing large and fast drifts due to the equatorial ionospheric anomaly. Moreover, TIDs are detected in the daytime, and the HTHH volcano eruption occurs during the recovery phase of a moderate geomagnetic storm. During the event, disturbance on the electric field is responsible for generating the westward equatorial electrojet

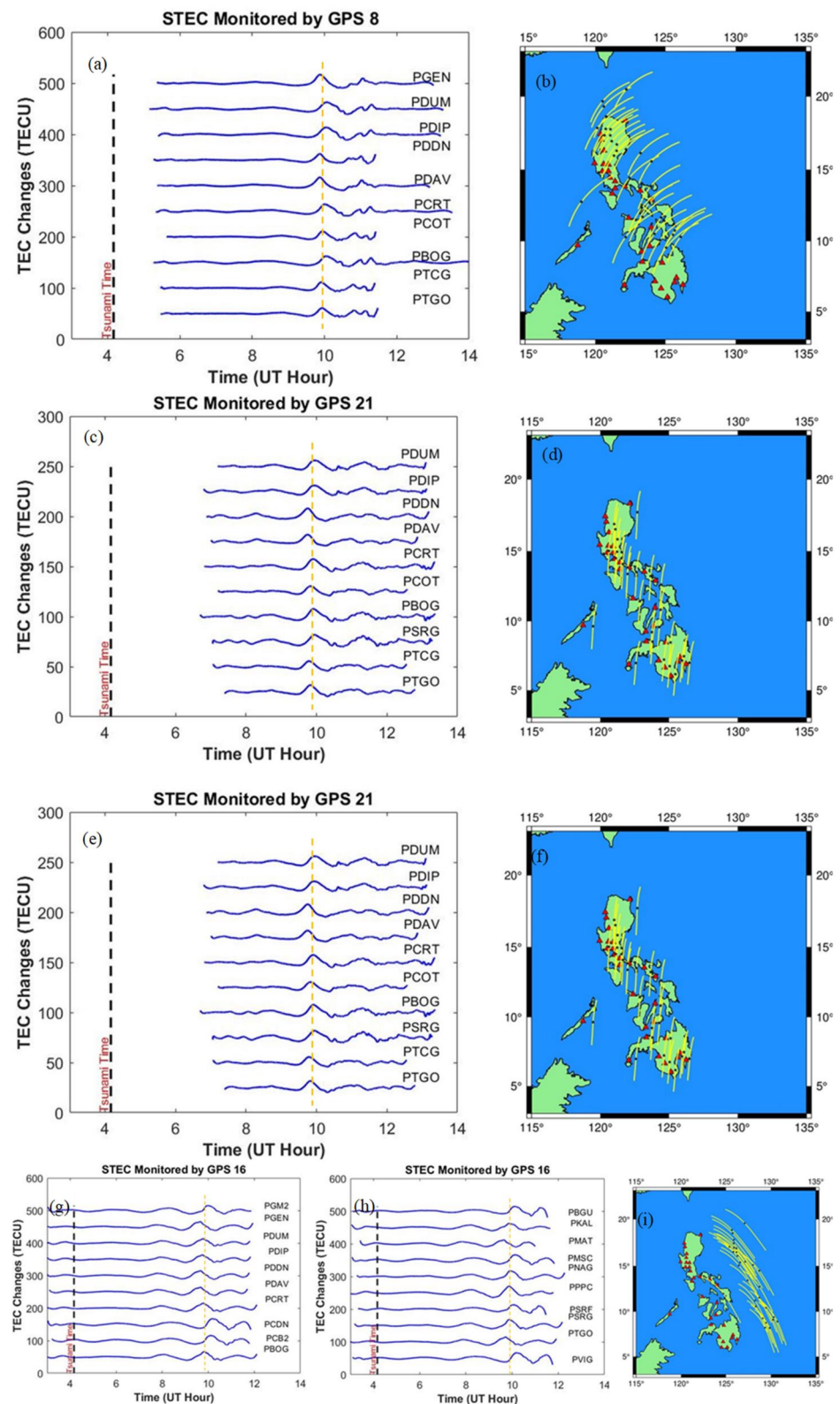


Figure 5. Time series of TEC residual (a,c,e,g,h) and SIP trajectory (b,d,f,i) in the Philippines. The black dashed lines in the time series indicate the timing of eruption; red triangles, the location of stations; yellow dashed lines in the time series, the peak of TIDs; yellow line, the trajectory of SIP at 08:00–10:00 UT; and black dots, the SIP when TIDs were detected.

(EEJ) (Zhang et al., 2021, 2022b). Previous research (Aa et al., 2022; Astafyeva et al., 2022; Li et al., 2023) stated that geomagnetic storms might affect TEC, although its effect might be insignificant. In addition, Le et al. (2022) stated that the eruption and the geomagnetic storm reversed the neutral wind direction. During the daytime, electric field (E) and magnetic field (B) interactions result in Lorentz force ($E \times B$), lifting the particles upward, called ionospheric radial current (IRC) (Muafiry & Heki, 2020; Qiu et al., 2019). Changes in IRC variations are influenced by prompt penetration electric field (PPEF) and neutral wind during geomagnetic storms. Increased PPEF during geomagnetic storms also affects the EEJ (Zhong et al. (2023)). The northward movement of the Earth's magnetic field and the eastward movement of the electric field cause upward movements of the ionosphere (Heki & Ping, 2005; Huang, 2020) along the geomagnetic equator. The upward movement of the ionosphere compresses the electron density, increasing the TEC. It also supports a westward neutral wind perturbation, reinforcing the background westward wind in the dayside and increasing the eastward electric field (Wang et al., 2022; Zhang, Wang, et al., 2022). Hence, the superposition between atmospheric waves, EEJ, and a small impact from a geomagnetic storm could influence the amplitude of TIDs in the Philippines (along the equator in the geomagnetic field in Table 1). This causes the TEC in the Philippines to become greater. Meanwhile, in high geomagnetic latitude areas, such as New Zealand and Australia, the influence of changes in the neutral wind direction is insignificant. The disturbance of dynamo electric fields has delayed responses to high-latitude heating events (Fuller-Rowell et al., 2002; Richmond & Matsushita, 1975; Scherliess & Fejer, 1997). In addition, Chen et al. (2023) observed that the impact of solar and geomagnetic activities on the ionosphere in Australia and New Zealand was limited and negligible. For this reason, New Zealand and Australia's TEC have a smaller amplitude than the Philippines.

Furthermore, on GPS satellite PRN 16 and 26 observations, the TIDs are at the end of satellite observations. This is because we used all satellites with no threshold or null elevation angles. This can be seen from the SIP position, which is far from the zenith station. This is already validated by the slant changes of TEC 1 day prior to and after the eruption, which showed the moderate variation, as presented in Figure S7 in Supporting Information S1.

Figure S8 in Supporting Information S1 presents the TIDs detected by GPS satellites 8, 16, 21, and 26, along with the positions of the SIP points from 09:36 to 10:24 UT and the corresponding dTEC values observed. TIDs appeared to take longer to reach the stations in the Philippines compared with those in cases 1 and 2, possibly because the distance from mainland Philippines is greater. Specifically, at around 09:30 UT, a positive dTEC moved in a southwesterly direction from the northeast, gradually dissipating until it disappeared at 10:30 UT.

Our study shows that the raw sTEC change measurements massively fluctuate, resembling a large W-shape (Astafyeva et al., 2022; Munaibari et al., 2023). Our estimation time series model (Figure 3) exhibited a pattern similar to that Zhang, Vierinen, et al. (2022) observed in New Zealand. SW and LW triggering TIDs (around 06:00 UT in New Zealand) resembles the TIDs induced by the GW (around 08:00 UT in New Zealand). However, the SW and LW signature exhibits a larger amplitude than the GW signature, which agrees with the previous research by Munaibari et al., 2023; Zhang, Vierinen, et al., 2022; Aa et al., 2022; etc. After reaching the maximum peak, the sTEC changes were followed by oscillations and small peaks. Astafyeva et al. (2022) suggest that the small peaks were caused by small eruptions after the large explosion.

3.2. Propagation Speed

Research on HTHH TIDs due to LW has been evaluated by Zhang, Vierinen, et al. (2022). They found TIDs with a primary speed of ~300–350 m/s that traveled worldwide three times. The global TIDs propagation is consistent with the effect of LW that have the speed of sound. Research into Hunga Tonga due to LW was also examined by Ghent and Crowell (2022) and Hu et al. (2023), who found that supersonic acoustic waves, LW, and tsunamis waves caused complex global ionospheric disturbances. Supersonic acoustic waves traveling at 833 m/s between 1,600 and ~3,000 km from Hunga arrive at a LW TIDs traveling at 310 m/s and are followed by a TIDs tsunami traveling at the same speed. Specific frequencies differentiate LW from tsunamis. Figure S12 in Supporting Information S1 shows the spectrogram obtained by the Blackman–Tukey method using the TEC time series by GPS 32 from TGTK station. The observed peak frequencies were ~0.476 mHz at 06:00 UT. In addition, the second TIDs at 08:00 UT obtained frequency values around 1.666 mHz consistent with the IGW. These frequencies concur with Hu et al. (2023) at the same research. However, the LW signature has a larger TIDs

amplitude than the tsunami classic signature. The difference in pressure originating from the AW (~6.5 hPa) at 06:00 UT and IGW (0.2 hPa) at 08:00 UT causes differences in the TIDs amplitudes as seen in Figure S3 in Supporting Information S1. The amplitude of TIDs due to AW (~5 TECU) is greater than the amplitude of TIDs due to tsunami (~1.68 TECU). This has been confirmed by Munaibari et al. (2023) in the same study. The LW also triggers an IGW, which propagates upward to the height of the ionosphere with the same horizontal speed as the LW (Munaibari et al., 2023). Heki (2022) also reported that the 2022 Tonga eruption produced a LW with a speed of 0.3 km/s, whereas those that typically propagated in the troposphere were at the speeds of sound between 300 and 350 m/s. Moreover, Themens et al. (2022) noted that the energy of LW is mainly confined to the troposphere, but their amplitude has the ability to increase exponentially with altitude due to the decrease in density. Similar to sound and gravitational waves, wave energy can escape to the upper atmosphere when LW resonate with the atmosphere at a horizontal phase velocity of approximately 300 m/s (Zhang, Vierinen, et al., 2022). It was also observed by Taylor (1932) that LW were associated with eruption events, such as the Mount Krakatoa eruption.

In this study, we analyzed TIDs that caused electron density in the ionosphere due to Atmospheric waves and tsunamis during the HTHH eruption on 15 January 2022. We observed TIDs spatially and temporally in three different regions using the 3D tomography method. The modeling results provided clear mechanisms and directivity. We observed an increase in electron density depicted in the time series of each region. The TIDs in New Zealand were observed to have three peaks at approximately ~06:00 and ~08:00 UT. The TIDs that appeared at around 06:00 UT had a period of approximately more than 30 min caused by SW and LW, which was explained in subsection 3.1. On the other hand, TIDs at around 08:00 UT had a shorter period of about 10 min caused by tsunami gravity waves that induce by tsunami classic. We also observed TIDs in the Australian region, which were observed at approximately 08:00 UT with a period of about 40 min. Lastly, we observed TIDs in the Philippines, which were detected at around 10:30 UT with a period of about 50 min. Our observations are consistent with those by Zhang, Vierinen, et al. (2022), who observed TIDs in New Zealand as a result of LW with period fluctuations of around 10–30 min.

Velocity was also calculated from ionospheric disturbances observed using least squares method and the TIDs distance from the eruption source was plotted against the propagation time using a travel time diagram. Figure S9 in Supporting Information S1 presents the observed TIDs travel time diagram in the New Zealand region using GPS satellites and the movement of the distance from the source of eruption with the observed TEC values. The positive dTEC values in red first appeared at around 05:70–06:10 UT, followed by negative values in blue. The velocity of the observed TIDs were 0.478, 0.301, 0.598, 0.545, 0.692, and 0.688 km/s for GPS satellites 10, 18, 23, 24, and 32 and GLONASS 47, respectively. This speed is consistent with Hu et al. (2023), where SW propagates at speeds up to ~1 km/s. The further the wave speed moves away, the weaker it becomes as shown in Figure S9 in Supporting Information S1 (e.g., GPS 32). First TIDs was caused by a SW with a speed of ~0.451 km/s at around ~06:00 UT. Then at 06:30 UT the TIDs propagated ~0.387 km/s. We also calculated the propagation velocity of the second TIDs at ~08:00 UT over New Zealand. The speeds obtained are ~0.311 and 0.246 km/s. This value is consistent with the IGW speed induced by the classic tsunami due to eruption water displacement (Hu et al., 2023). Furthermore, Figure S10 in Supporting Information S1 presents the travel time for the GPS satellites, and the results were recorded to be 0.337, 0.312, and 0.313 km/s for GPS satellites 10, 21, and 32, respectively. Figure S11 in Supporting Information S1 also presents the travel time for the GPS satellites in the Philippines, which were 0.490, 0.446, 0.561, and 0.497 km/s for GPS satellites 8, 16, 21, and 26, respectively. It is clearly enough to assume that the tsunami resulting from the HTHH eruption was caused by AW and due to water displacement eruptions. Apart from causing tsunamis, AW also cause TIDs in the ionosphere, with the wave speed getting weaker the further away it is.

4. 3D Ionospheric Disturbances

The 3D ionospheric disturbances caused by the 2022 HTHH eruption were further studied using GNSS TEC. The modeling was focused on an altitude of 100–600 km with a coverage area that matches the model from the checkerboard resolution test. Furthermore, the 3D tomography model was designed for spatial and temporal analyses from an elevation interval of 100 km in a time interval of 6 min. This model has been previously used by Muafiry and Heki (2020) to analyze ionospheric disturbances before the earthquake in Japan, and the results indicated that the anomaly was visible sometime before the earthquake occurred. He and Heki (2018) also applied the same method to ionospheric disturbances caused by the 2015 Chile earthquake. Therefore, this model was

applied in this study to provide an overview of ionospheric disturbances caused by the SW and LW induced by the 2022 HTHH eruption.

4.1. 3D Tomography in New Zealand

A 3D tomography model was created from 05:42 to 06:48 UT to observe ionospheric disturbances in the New Zealand region at several altitudes using a six-layer arrangement with an interval of 100 km; the results are presented as follows.

Figure 6 presents a 3D tomography model of the New Zealand region from 05:42 to 06:48 UT at an altitude of 100–600 km, and it was found that the positive dTEC in red first appeared at 05:48 UT and was detected at an altitude layer of 300 km. It became more visible at 05:54 UT at 200-, 300-, and 400-km layers with the most solid values recorded at 300 km. At the time, TIDs were observed to be moving to the southwest in line with the direction of the tsunami in Figure 1. At 06:00 UT, the 300-km altitude layer looked the most colorful, indicating that the TIDs were at their maximum value. It was later observed from 06:06 to 06:18 that the positive dTEC value gradually decreased due to the deficiency of data on TIDs in the zone and the inhibition of the tsunami propagation when it hit mainland New Zealand. This was indicated by the appearance of the positive dTEC in red blocks in the 3D tomography model from 05:42 to 06:12 UT and its subsequent disappearance at 06:18 UT. The negative dTEC in blue blocks also started appearing and moving at 06:18 from the northeast, which was the source of the tsunami, in the same direction as the positive dTEC and disappeared at 06:48 UT.

The sign of an ionospheric hole can be observed in the 3D tomography results in Figure 7 at 06:18–06:48 UT. As can be seen from the figure, there is a decrease in the TEC change value, which is marked with a blue voxel. This ionospheric hole is moving toward the southwest. Our results are similar to the ionospheric holes found by Aa et al. (2022) and Astafyeva et al. (2022), which appeared 1–2 hr after the eruption in an area as far as 2000 km from the epicenter. Positive and negative dTEC waves are two types of waves that occur as a result of ionospheric disturbances. These disturbances can be caused by oscillations of waves that go up and down before returning to normal conditions. The physical mechanism of positive anomaly waves starts when there is an increase in electron density in the ionospheric layer, caused by a LW. After rising, this wave starts to descend, resulting in a decrease in electron density. When these wave oscillations return to the normal state, the electron density in the ionospheric layer also returns to normal. Anomalous positive and negative waves are two types of waves that occur as a result of ionospheric disturbances. This disturbance can be caused by oscillating waves that rise and fall before returning to normal conditions. The physical mechanism of anomalous positive waves starts when there is an increase in electron density in the ionosphere, which is caused by a slow wave. After rising, these waves begin to fall again, which results in a decrease in electron density. When these wave oscillations return to normal conditions, the electron density in the ionosphere also returns to normal.

4.2. 3D Tomography in Australia

3D tomography modeling of ionospheric disturbances for the Australian region was conducted from 06:48 to 07:36 UT at an altitude of 100–600 km arranged at an interval of 100-km altitude.

Figure 8 presents the 3D tomography model in the Australian region from 06:48 to 07:36 UT at an altitude of 100–600 km. Meanwhile, Figure 9 presents the appearance of the positive dTEC from the east, which is the source of the tsunami, and its movement toward the southwest at 07:00 UT. The movement of ionospheric disturbances was found to be in the same direction as the New Zealand region. The peak of the dTEC was recorded at 07:30 UT, and the negative dTEC was at 07:36 UT in line with the movement of the positive dTEC. The consistent observation was that the 300-km altitude had a brighter value than the other altitudes due to the assumption of maximum ionization at the point based on the Chapman model (1931), as will be discussed later. In simple terms, ionospheric disturbances started reducing at altitudes of 200 and 400 km.

4.3. 3D Tomography in the Philippines

3D tomography ionospheric modeling was conducted in the Philippines at 09:36–10:24 UT, as presented in Figure 10. The time range was selected based on TIDs in the ionosphere layer when viewed from the time-series graph. The positive dTEC appeared at 09:36 UT from the east of the country, which was the direction of the tsunami, and later moved to the northwest.

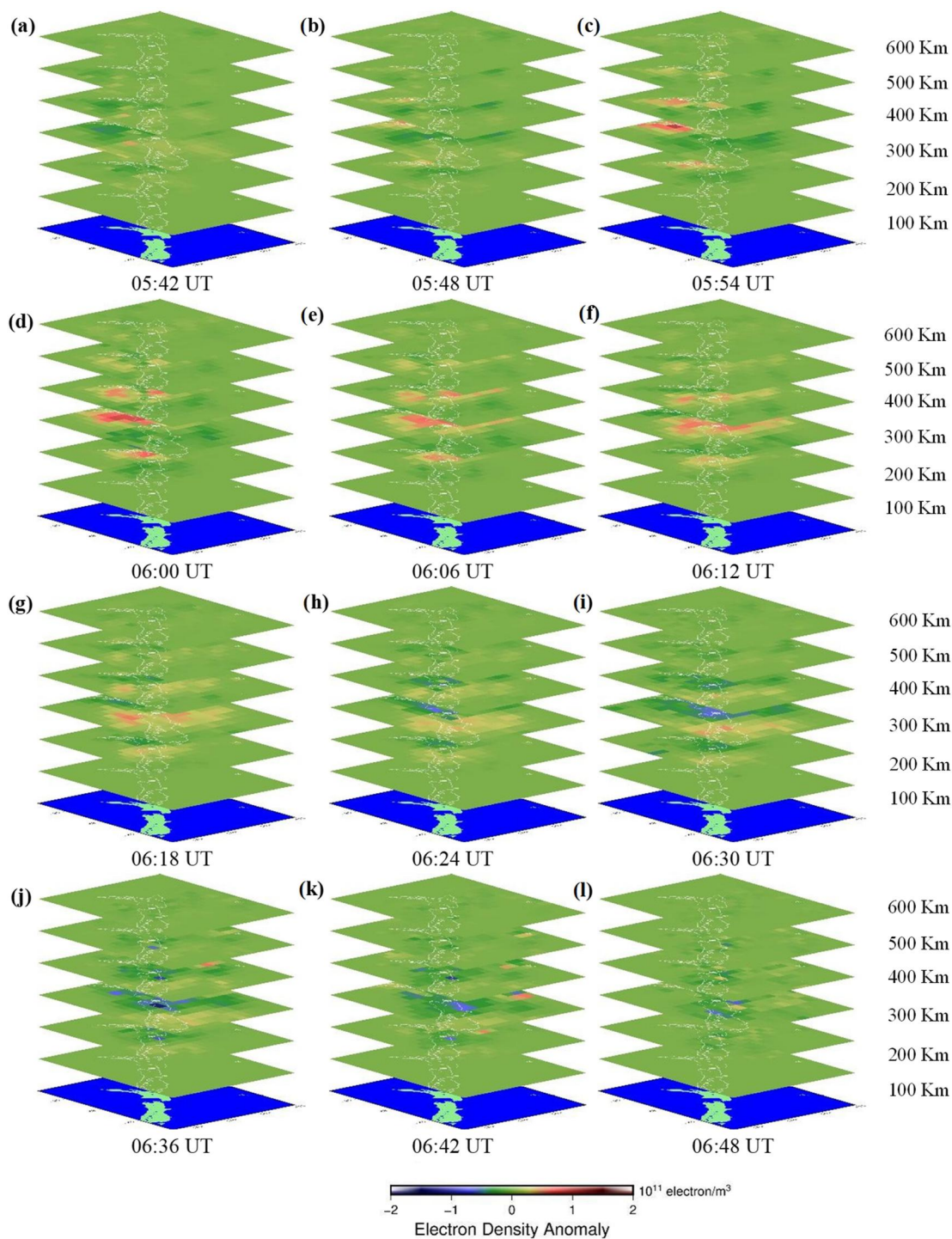


Figure 6. Distribution of 3D tomography ionospheric disturbances in New Zealand.

A positive dTEC occurred for a few minutes and was followed by a negative dTEC or ionospheric hole shown in dark green to the east of the positive dTEC. The maximum electron density at 300 km is presented in Figure 10, whereas the emergence of the positive dTEC from the satellite at the east of the mainland Philippines and subsequent movement toward the mainland to the northwest, which is the direction of the tsunami, are presented in Figure 11.

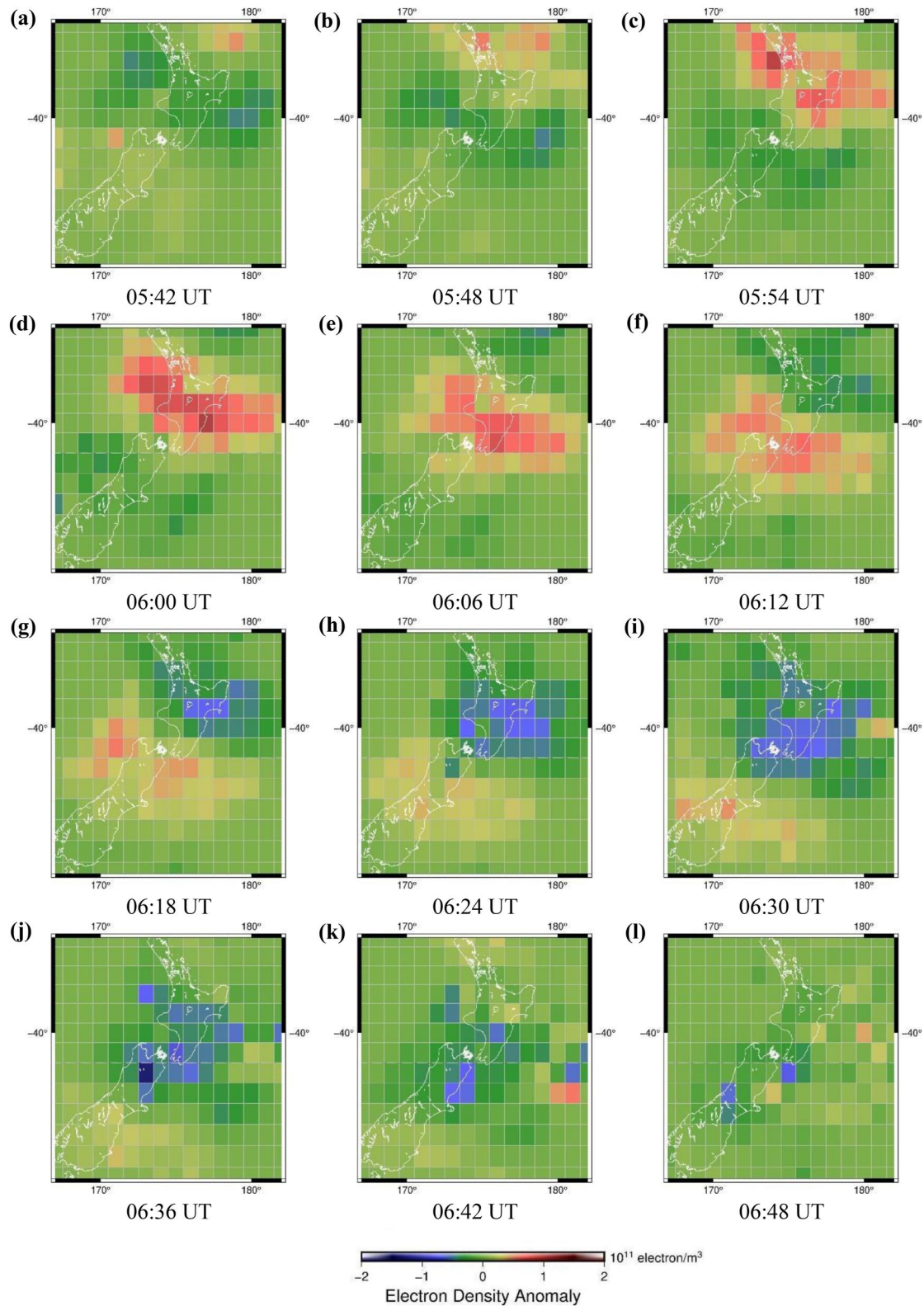


Figure 7. Allocation of tomography ionospheric disturbances at 300 km. It is shown that the directivities of TIDs were in the southwest.

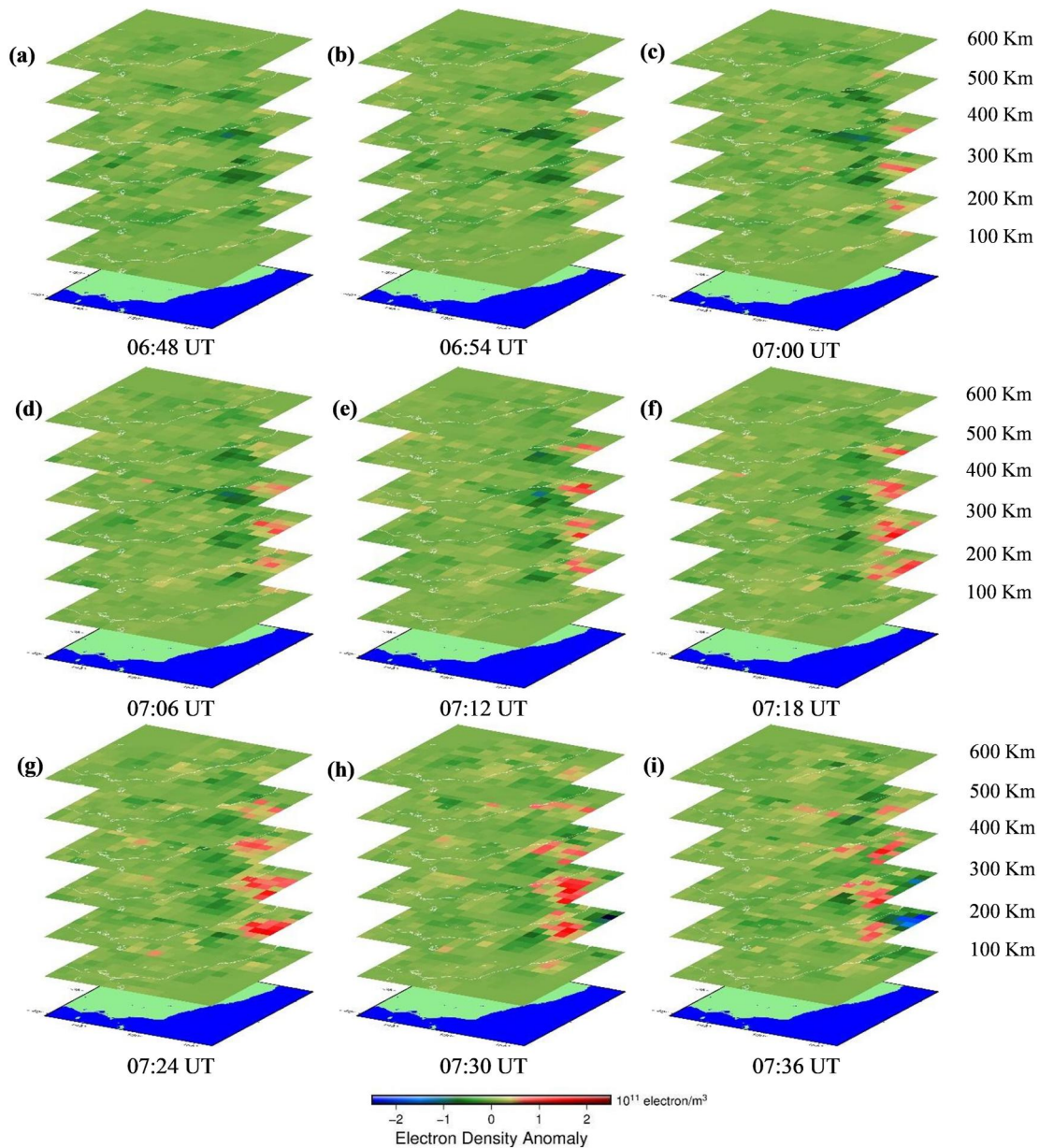


Figure 8. Distribution of 3D tomography ionospheric disturbances in Australia.

Heki (2022) analyzed TIDS caused by the HTHH tsunami using the data from QZSS-TEC observed in Japan and found that the disturbances propagated westward at a rate of approximately 0.3 km/s, with the wavefront parallel to the contour of the geomagnetic conjugate domain of the volcano. The findings of this study also indicated a westward movement of ionospheric disturbances in the Philippines, suggesting the consistency of the 3D tomography modeling applied to the findings of previous studies. The results of the 3D tomography modeling for each layer showed an anomaly that started with a positive dTEC value indicated by a cream-red voxel moving toward the direction of the tsunami and a LW moving concentrically from the center of the explosion. These were followed by a negative colored dTEC represented using a hole marked with a dark green–blue voxel moving in the same direction as the peak TIDs which are represented by the red voxels. At the beginning of the modeling period, the positive dTEC was faintly preceded by a negative dTEC shown as a dark-green voxel. Furthermore, the decrease in the dTEC was found to be insignificant, but the dTEC later significantly increased and then decreased

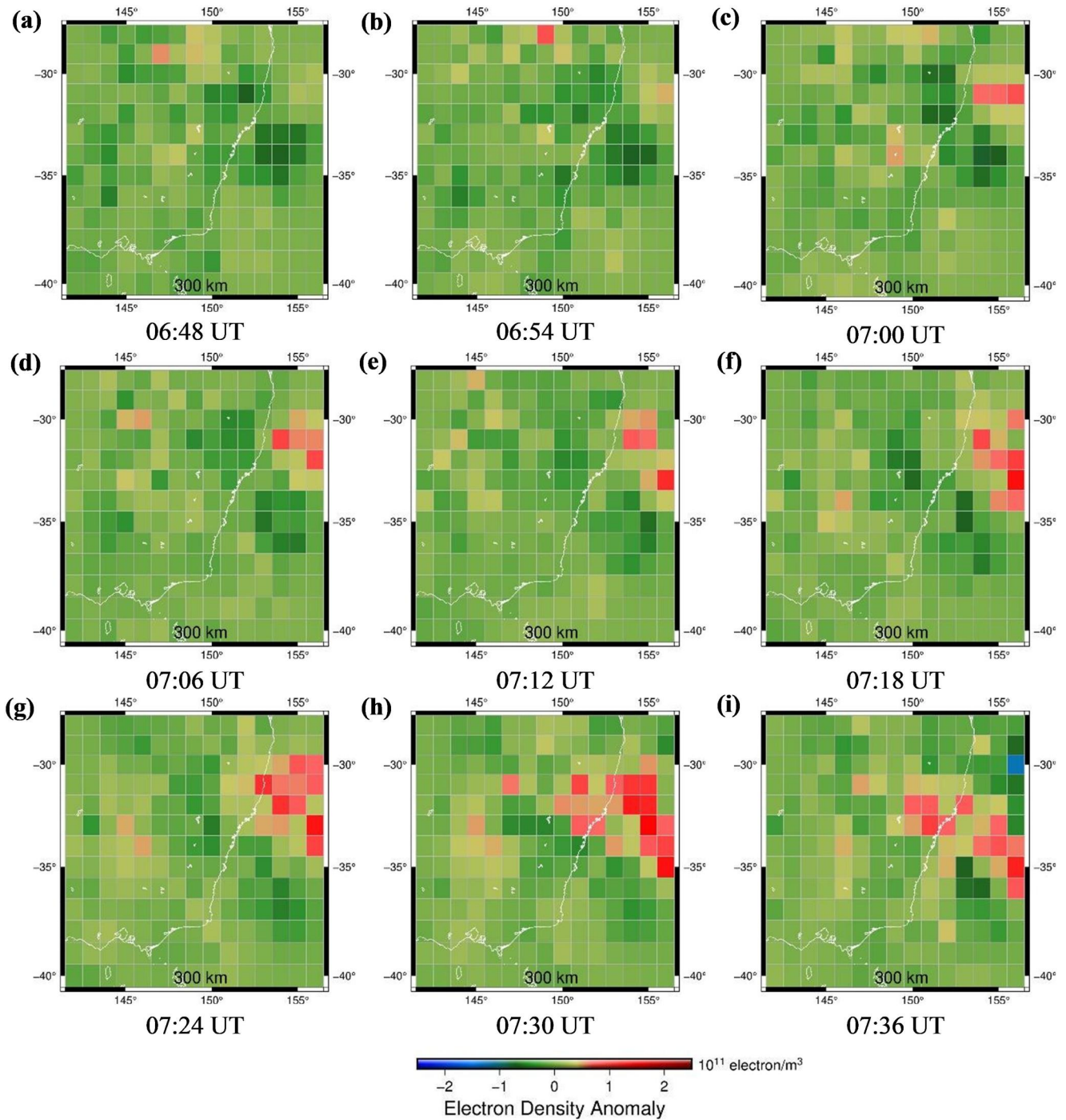


Figure 9. Allocation of a tomography ionospheric disturbances at 300 km. It is shown that the directivities of TIDs were in the southwest (SW).

to form a negative–positive–negative pattern like the W shape. This is consistent with the results of a previous study conducted by Munaibari et al. (2023).

The modeling results indicated that the maximum electron density was at an altitude of 300 km, and this was attributed to the use of two constraints in the modeling process including continuity and altitude-dependent constraints based on the Chapman model. The continuity constraint assumes that neighboring voxels have relative voxels passing through LoS at a tolerance of $0.10 \times 10^{11} \text{ el/m}^3$, with the uniform STEC error

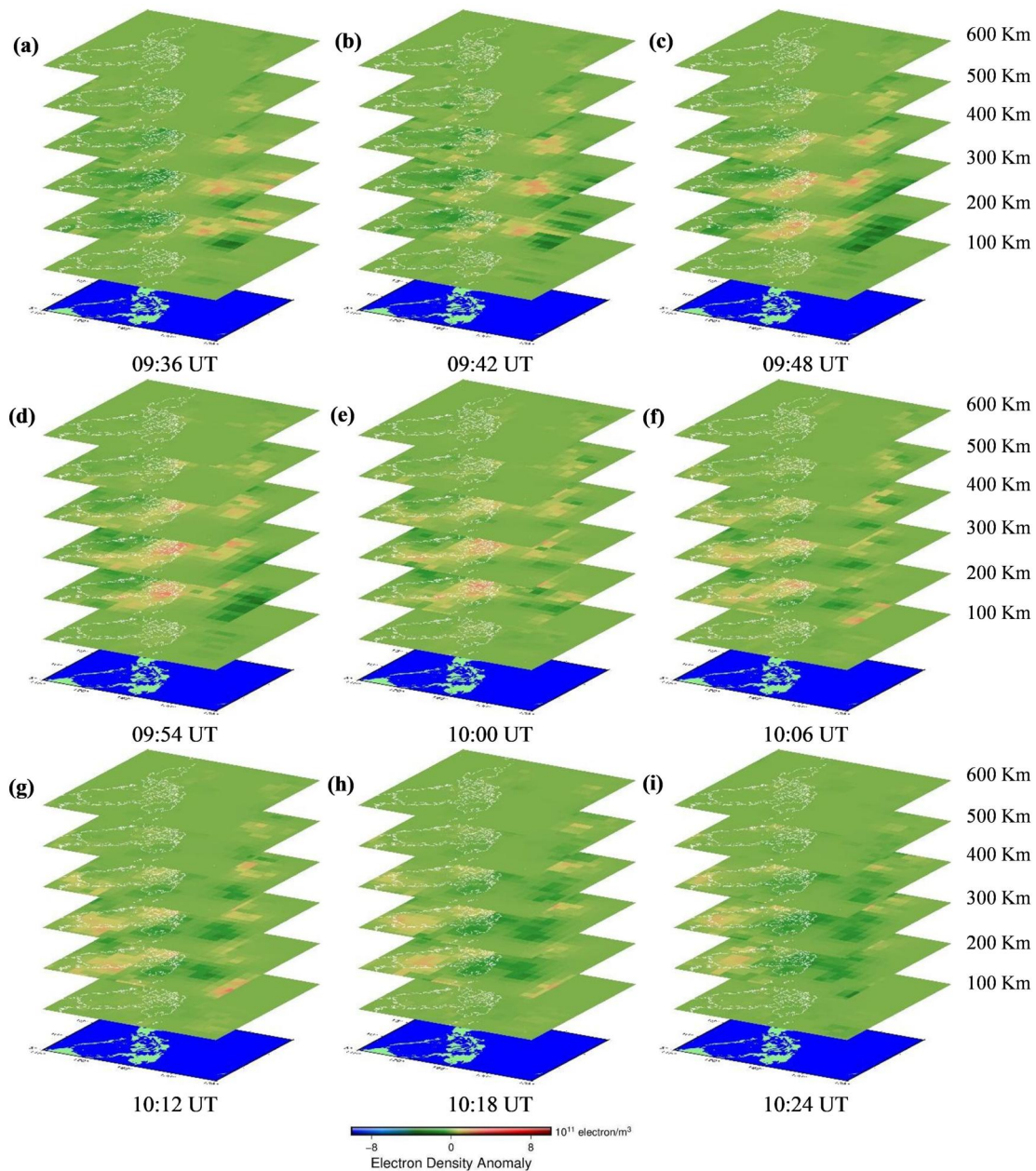


Figure 10. Distribution of 3D tomography ionospheric disturbances in the Philippines.

assumed to be 0.2 TECU, where 1 TECU is 10^{16} el/m². Heavily dependent constraints were used to provide more realistic modeling results to avoid estimation of unrealistically large electron-density dTEC at very high or very low altitudes. The height-dependent constraints were based on the Chapman model, which assumes a maximum ionization at ~ 300 km. Therefore, the results obtained from the model were more realistic and follow the Chapman model (1931). The vertical profile of electron density was also estimated on 15 January 2022, and the time TIDs occurred in each location using the IRI model (<https://irimodel.org/>). The results indicated that the highest electron density was at an altitude of ~ 280 – 350 km, as presented in Figure 12, and this is in line with the 3D tomography modeling applied at the height of the third ionospheric layer with an altitude of ~ 300 km (Chapman, 1931). The results obtained in this study are consistent with those in the study by Shinbori et al. (2022), which indicated that the electron density calculated as a function of time had

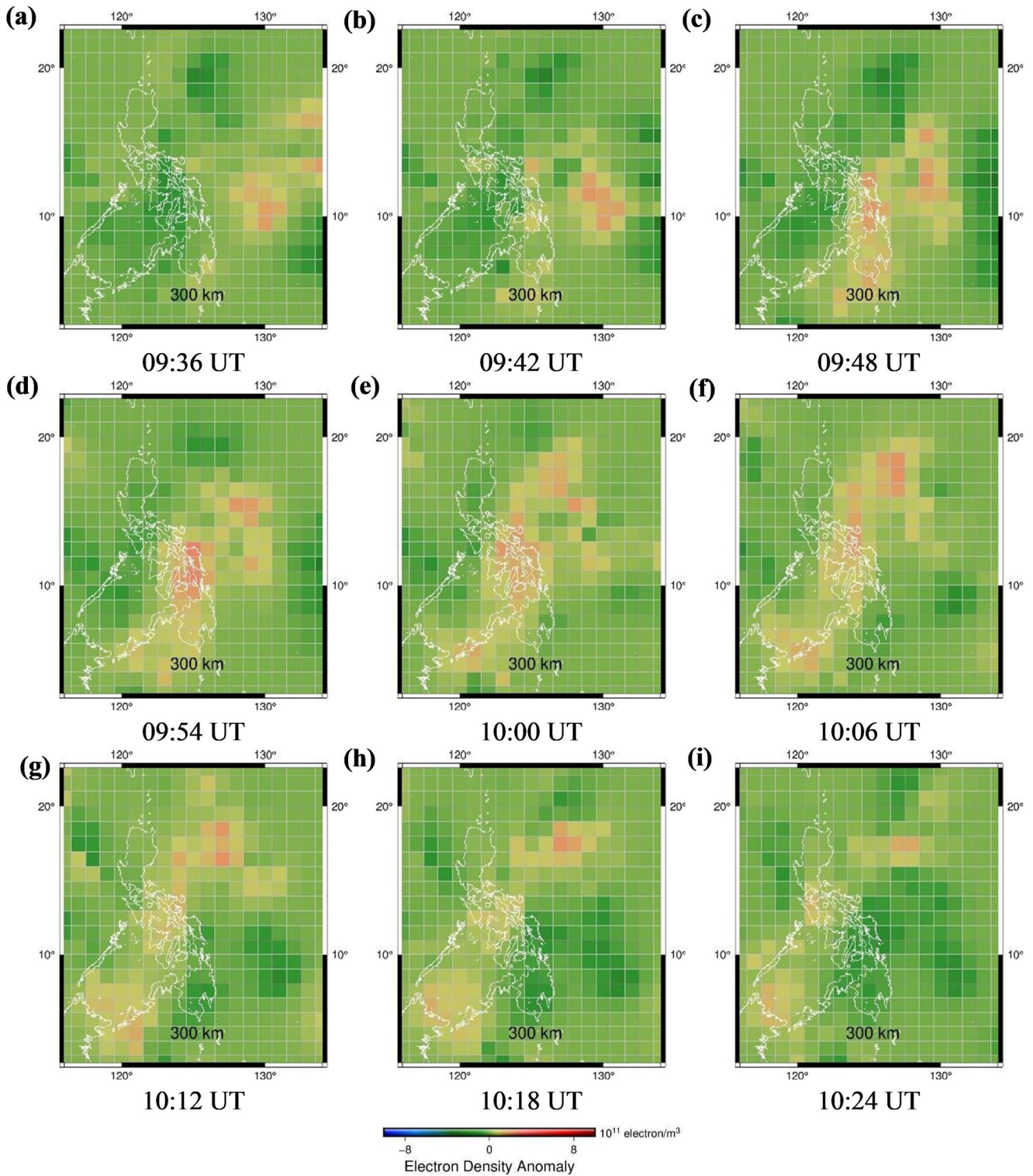


Figure 11. Allocation of tomography ionospheric disturbances at 300 km. It is shown that the directivities of TIDs were in the northwest.

a peak altitude of ~ 300 km. Furthermore, the adaptability of 3D tomography extends to observing the effects of SW and LW at altitudes of up to ~ 500 km. These observations align seamlessly with data acquired through radio occultation methods, where TIDs can reach up to ~ 500 km altitude, as reported by Shinagawa

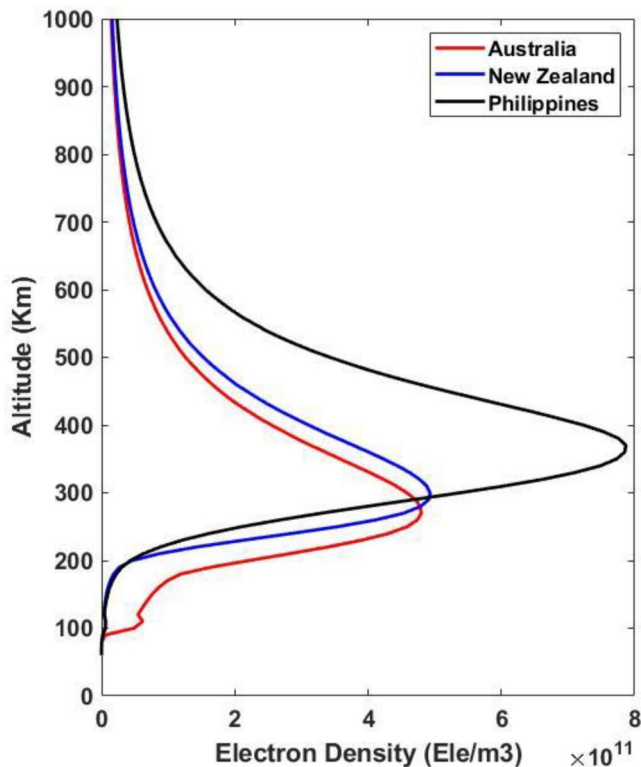


Figure 12. Vertical electron-density profiles reconstructed on TIDs using the IRI model (<https://irimodel.org/>).

and Miyoshi (2023). This alignment provides crucial validation for radio occultation data, thereby enhancing and fortifying our comprehension of TIDs at elevated altitudes.

4.4. Directivity of TIDs

The results of the 3D tomography modeling conducted in New Zealand and Australia located in the southwest of Tonga indicated that the movement of TIDs was preceded by a positive dTEC, followed by a negative dTEC or ionospheric hole in the direction of the tsunami. It is noteworthy that the tsunami waves hit mainland New Zealand and Australia from the northeast to the southwest, as presented in Figures S3 and S4 in Supporting Information S1, and TIDs also moved in the same direction. These results were consistent with those recorded with the 2D dTEC distribution model, where the SIP marked a southward propagation through a red arrow at 0.3 km/s as reported by Zhang, Vierinen, et al. (2022).

The directivities of TIDs for Australia and New Zealand were toward the southwest, whereas that of the Philippines was in the northwest. Notably, the Philippines is geographically located in the northwest of HTHH; this is the reason why the tsunami waves and directivity of ionospheric disturbances were propagated toward the direction. Meanwhile, the directivity produced for the three case studies by the 3D tomography modeling was similar to that of the tsunami. It was observed that TIDs appeared from the east of the mainlands, crashed, and then moved away in the direction of the arrival of the tsunami. These results are consistent with those in the study by Aa et al. (2022), Saito (2022), Heki (2022), and Zhang, Vierinen, et al. (2022), which indicated that TIDs moved in the south–southwestward direction or radially outward in the same direction away from the epicenter.

5. Checkerboard Validation

The 3D tomography model and its electron densities were validated using the checkerboard resolution test. Furthermore, the changes in the ionosphere during the 2022 Tonga tsunami were investigated, and the dTEC data were synthesized based on the assumption that the electron-density dTEC was allocated as boxes with 0.50 and -0.50 TECU/100 km. It is noteworthy that Muafiry et al. (2018) and Muafiry and Heki (2020) as well as Cahyadi et al. (2020, 2022a) have previously used the 3D tomography test with the checkerboard test model.

The TIDs distribution determined by the checkerboard data synthesis model for New Zealand is presented in Figure 13b. It was found that the 3D tomography perfectly captured the tall structures, as presented in input Figure 13a. Furthermore, comparison of the two output displays showed that the resolution was high at higher altitudes ~ 200 km. The result shows at least 61% of the total area that can invert the input values well, higher over land and lower over the ocean as indicated in the output image due to the limitation of the data (LoS).

The same model was used in the Australian region, as presented in Figure 14, and the value produced almost covered 2/3 of the entire area. The model was tested at an estimated altitude of 200 km and was found to have the ability to effectively invert synthetic models with an inversion of more than 2/3 of the studies indicated by Muafiry et al., (2018). It was found that several areas above the ocean were not effectively covered due to the lack of data on these areas.

The checkerboard test conducted in the Philippines case study did not produce synthesis data as good as those in Australia and New Zealand, as shown in Figure 15. The result shows only 35% of the total area that can invert the model. This could be attributed to the limited data obtained from only 33 stations, which complicated the testing process. Constraints as well as trial and error were applied to obtain the maximum model in this area.

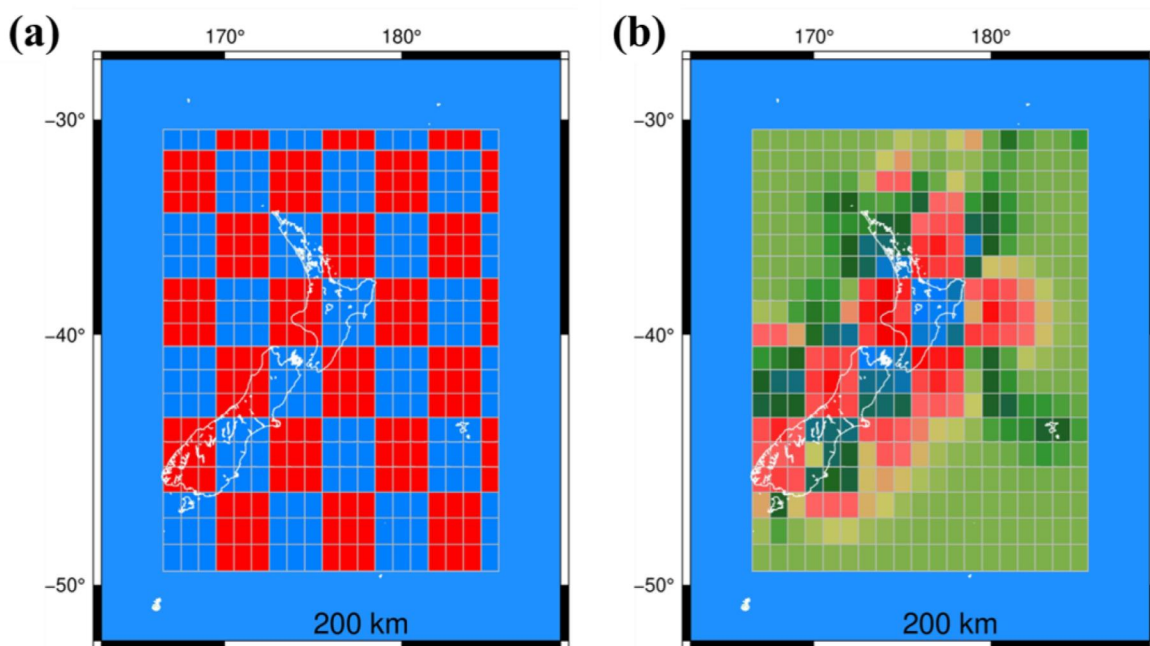


Figure 13. Checkerboard resolution test of the tomography model in New Zealand. A TIDs scheme of electron density was used with a height of 200 km. The input (a) was formed by synthetic data and the output (b) by the results of the inversion calculation using the observation data.

6. Discussion

Research on ionospheric disturbances caused by tsunamis and other phenomena has been conducted by Kamogawa et al. (2016), Rakoto et al. (2017), and Savastano et al. (2017), who showed a correlation between the magnitude of the ionospheric disturbance and the height of the tsunami. Therefore, an attempt was made to analyze the correlation between the tsunami amplitude measured using DART (Gusman & Roger, 2022) and TIDs amplitude calculated using GNSS TEC. The tsunami height model was obtained by interpolating the DART data using kriging method is presented in the following Figure 16. The tsunami we modeled was triggered by SW and

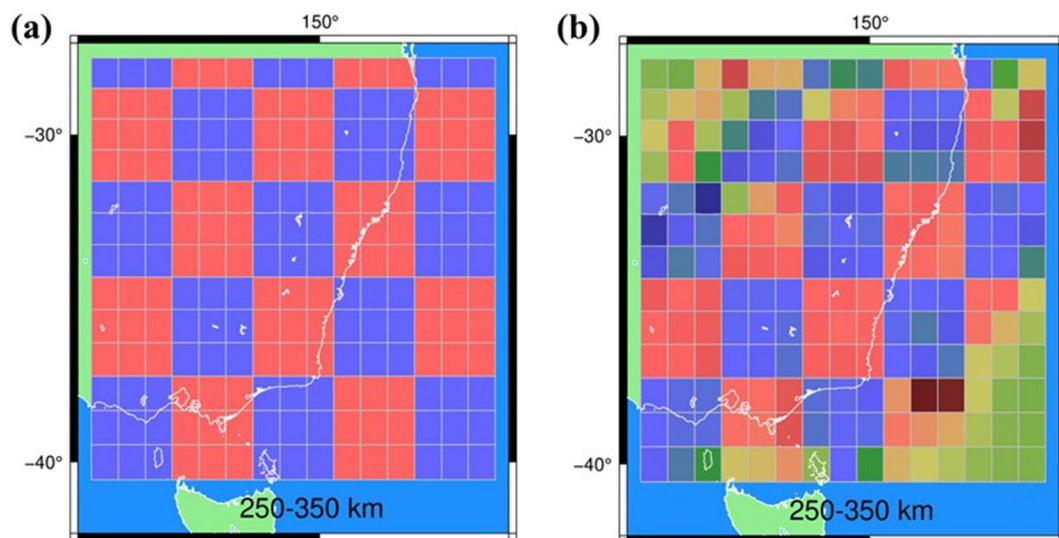


Figure 14. Checkerboard resolution test of the tomography model in Australia. A TIDs scheme of electron density was used with a height of 200 km. The input (a) was formed by synthetic data and the output (b) by the results of the inversion calculation using the observation data.

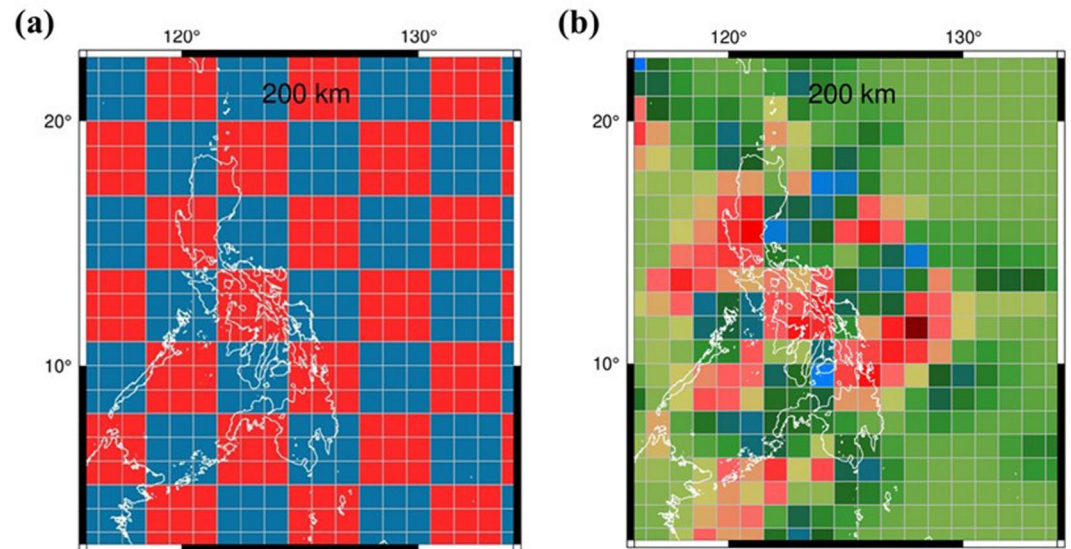


Figure 15. Checkerboard resolution test of the tomography model in the Philippines. A TIDs scheme of electron density was used with a height of 200 km. The input (a) was formed by synthetic data and the output (b) by the results of the inversion calculation using the observation data.

LW that occurred around 06:00 UT. Yellow star was used to indicate the location of the tsunami center (HTHH), whereas a small black circle represents the location of TIDs used as the test points.

The correlation between tsunami amplitude height and TEC amplitude value for TIDs was analyzed from ~105 SIP sample points spread across New Zealand and Australia. The TEC and DART data also have the same time and position as extracted by value from the tsunami model raster. It is noteworthy that the Philippines was not considered because the TIDs in this region were not purely produced by the tsunami but rather accumulated due to several phenomena. The tests conducted indicated that the correlation values for New Zealand and Australia were 0.64 and 0.65, respectively, and these were classified as moderate, as presented in Figure 17. Furthermore, the data collection timing for dTEC and DART was adjusted to the time the tsunami occurred in each region; this contributed to the fairly high value recorded in the correlation test.

Kamogawa et al. (2016) conducted a study that established a correlation between the height of a tsunami, magnitude of an earthquake, and percentage of TEC depression during an ionospheric disturbance. The study found a positive correlation between TEC depression and tsunami height. Similarly, Rakoto et al. (2017) evaluated the TEC values and tsunami heights in multiple tsunami cases, including the 2012 Haida Gwaii tsunami, 2006 Kuril Islands tsunami, and 2011 Tohoku tsunami. The findings showed an association between tsunami height and DTEC, where a higher DTEC value corresponded to a higher tsunami height value. In addition, Savastano et al. (2017) examined ionospheric disturbances resulting from the 2011 Tohoku Oki earthquake and the 2012 Emilia earthquake, and their results similarly showed that TIDs were consistent with the height of the tsunami model. Therefore, an attempt was made to analyze the correlation between the tsunami amplitude measured using DART (Gusman & Roger, 2022) and TIDs amplitude calculated using GNSS TEC.

The maximum TIDs was compared with the sea-level peaks, as presented in Figure 18. It was found that TIDs appeared 10 min earlier than the sea-level peaks in the New Zealand region and 8 min earlier in the Australian region. This led to the analysis of the consistent appearance of TIDs earlier than the sea-level rise, and the results were found to be the same as those reported by Savastano et al. (2017), who detected TEC perturbations before the actual tsunami arrival.

7. Conclusion

We observed TID after the HTHH eruption with GNSS TEC data in Australia, New Zealand, and the Philippines. The source is analyzed by calculating its speed using a time-distance diagram and a power spectrum. The first TID was generated by SW and LW at ~06:00 UT over New Zealand. The first one has a speed of ~0.692 km/s, and its

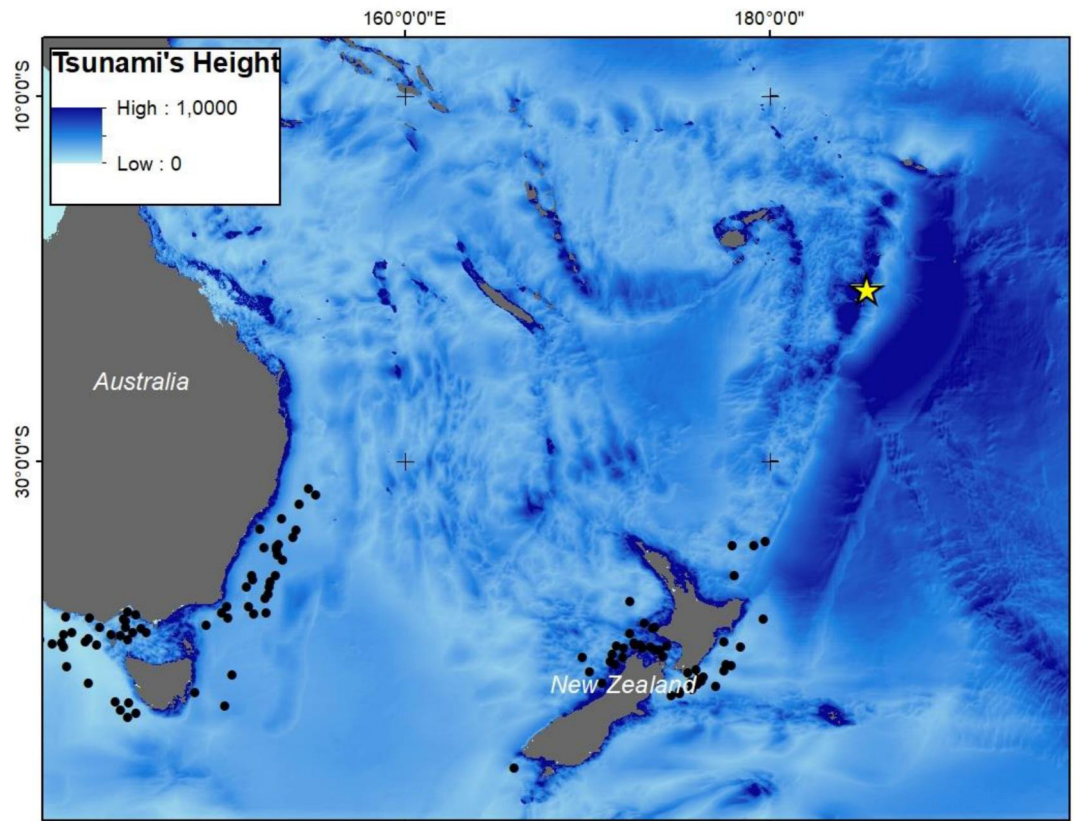


Figure 16. SIP location for correlation testing.

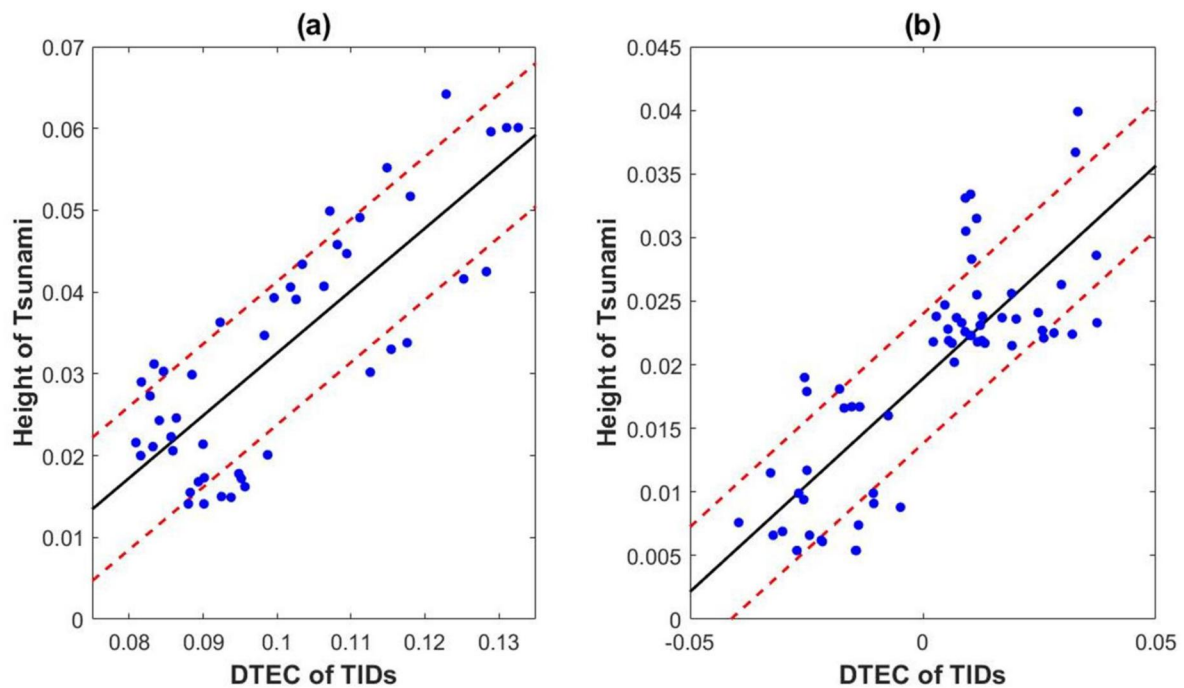


Figure 17. Comparison of TIDs values from several tsunami height test points in New Zealand (a) and Australia (b). The black and two red dashed lines indicate the regression and uncertainties of the factor by two errors, respectively.

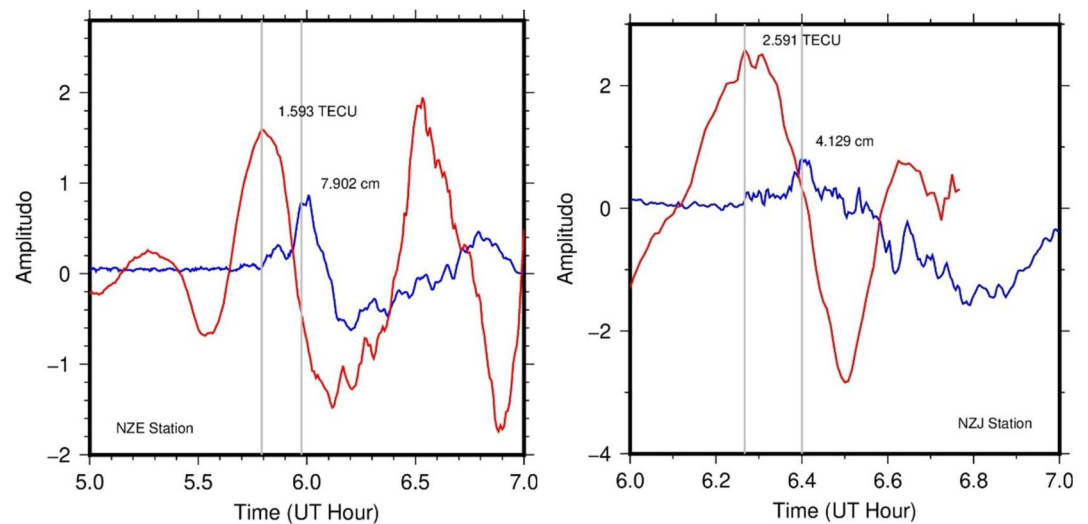


Figure 18. Time series between TEC (red line) and DART data (blue line), where the TEC time series uses the PRN 18 satellite from the ARTA station in New Zealand and the LORD station in Australia. Meanwhile, the DART time series uses the NZE station (for New Zealand) and the NZJ station (for Australia). The gray line indicates the peak time of the TEC and DART data.

speed decreases gradually. The final wave had a speed of ~ 0.3 km/s Gusman et al. (2022) reported that this atmospheric wave caused a tsunami wave at 06.00 UT. Interestingly, a moderate correlation was found between these tsunami waves and TID. A second TID discovered at $\sim 08:00$ UT generated by the IGW due to displacement of eruptive water has also been studied. This TID has a typical classical tsunami speed of ~ 200 m/s which is in line with Hu et al. (2023).

The 3D structure of the first TID after the HTHH eruption has also been analyzed using GNSS TEC data in Australia, New Zealand, and the Philippines. In New Zealand, the results of the analysis show that the first TID has a maximum concentration of oblique TEC changes at 200–300 km above the surface and begins to decrease at an altitude of 500–600 km. Shinagawa and Miyoshi (2023) also found that this TID can reach heights of up to ~ 500 km using the radio occultation method. Additionally, our 3D model shows the direction of the TID to be the same as the direction of the tsunami and atmospheric waves (spreading outward). Tomograms in Australia and the Philippines also showed the same TID results as in New Zealand. However, the tomogram in the Philippines is no better than the other two selected countries (e.g., only 35% of voxels were found) because GNSS stations on land are rare and limited. Nevertheless, our observations in the Philippines show large amplitudes of TEC obliquity changes due to LW accumulation, equatorial electrojet, EIA, tsunami, and geomagnetic storm effects on equatorial geomagnetics.

Data Availability Statement

All the data used in this study are available at the ARGN (<https://data.gnss.ga.gov.au/>) observation station in Australia, GeoNet (<https://data.geonet.org.nz/gnss/rinex/2022/015/>) in New Zealand, and PAGeNet in the Philippines (<https://pagenet.namria.gov.ph/SBC/spider-business-center>).

Acknowledgments

The authors appreciate the ARGN observation station in Australia, GeoNet in New Zealand, and the PAGeNet for providing GNSS data observation. They also show gratitude to the World Class Professor with Grant 3252/E4/DT.04.03/2022; Our Community Outreach (ORM) 2023; National Natural Science Foundation of China (NSFC) Project with Grant 12073012 and also by Penelitian Kemitraan ITS Batch 2 with Grant 1653/PKS/ITS/2022 for providing the fund.

References

- Aa, E., Zhang, S. R., Erickson, P. J., Vierinen, J., Coster, A. J., Goncharenko, L. P., et al. (2022). Significant ionospheric hole and equatorial plasma bubbles after the 2022 Tonga volcano eruption. *Space Weather*, 20(7), e2022SW003101. <https://doi.org/10.1029/2022sw003101>
- Abidin, H. Z. (2000). Penentuan posisi dengan GPS dan aplikasinya.
- Andrews, R. G. (2022). Tonga shock wave created tsunamis in two different oceans. *Science*. <https://doi.org/10.1126/science.ada0562>
- Anjasmara, I. M., Yulyta, S. A., Cahyadi, M. N., Khomsin, T. M., & Jaelani, L. M. (2018). *Land subsidence analysis in Surabaya urban area using time series InSAR method*. In *AIP Conference Proceedings* (Vol. 1987). AIP Publishing LLC. No. 1.020071.
- Astafyeva, E., Maletckii, B., Mikesell, T. D., Munaibari, E., Ravanelli, M., Coisson, P., et al. (2022). The 15 January 2022 Hunga Tonga eruption history as inferred from ionospheric observations. *Geophysical Research Letters*, 49(10), e2022GL098827. <https://doi.org/10.1029/2022gl098827>

- Cahyadi, M., & Heki, K. (2013a). The scaling law of the near-field coseismic ionospheric disturbances. In *AGU Fall Meeting Abstracts* (Vol. 2013, pp. NH13C-1625).
- Cahyadi, M. N. (2014). *Near-field coseismic ionospheric disturbances of earthquakes in and around Indonesia*. (The Degree of Doctor of Philosophy). Dept. Natural History Sciences, Graduate School of Science, Hokkaido University.
- Cahyadi, M. N., Anjasmara, I. M., Khomsin, Y. M., Sari, A., Saputra, F. A., et al. (2018). *Coseismic ionospheric disturbances (CID) after West Sumatra earthquake 2016 using GNSS-TEC and possibility of early warning system during the event*. In *AIP Conference Proceedings* (Vol. 1987). AIP Publishing LLC. No. 1.020019.
- Cahyadi, M. N., Arisa, D., Muafiry, I. N., Muslim, B., Rahayu, R. W., Putra, M. E., et al. (2022a). Three-dimensional tomography of coseismic ionospheric disturbances following the 2018 Palu Earthquake and tsunami from GNSS measurements. *Frontiers in Astronomy and Space Sciences*, 9, 890603. <https://doi.org/10.3389/fspas.2022.890603>
- Cahyadi, M. N., Arisa, D., Muafiry, I. N., Muslim, B., Rahayu, R. W., Putra, M. E., et al. (2022b). Directivity of coseismic ionospheric disturbances propagation following the 2016 West Sumatra earthquake using three-dimensional tomography GNSS-TEC. *Atmosphere*, 13(9), 1532. <https://doi.org/10.3390/atmos13091532>
- Cahyadi, M. N., Handoko, E. Y., Rahayu, R. W., & Heki, K. (2021). Comparison of volcanic explosions in Japan using impulsive ionospheric disturbances. *Earth, Planets and Space*, 73(1), 1–8. <https://doi.org/10.1186/s40623-021-01539-5>
- Cahyadi, M. N., & Heki, K. (2013b). Ionospheric disturbances of the 2007 Bengkulu and the 2005 Nias earthquakes, Sumatra, observed with a regional GPS network. *Journal of Geophysical Research: Space Physics*, 118(4), 1777–1787. <https://doi.org/10.1002/jgra.50208>
- Cahyadi, M. N., & Heki, K. (2015). Coseismic ionospheric disturbance of the large strike-slip earthquakes in North Sumatra in 2012: M_w dependence of the disturbance amplitudes. *Geophysical Journal International*, 200(1), 116–129. <https://doi.org/10.1093/gji/ggu343>
- Cahyadi, M. N., Muslim, B., Pratomo, D. G., Anjasmara, I. M., Arisa, D., Rahayu, R. W., et al. (2022). Co-seismic ionospheric disturbances following the 2016 West Sumatra and 2018 Palu earthquakes from GPS and GLONASS measurements. *Remote Sensing*, 14(2), 401. <https://doi.org/10.3390/rs14020401>
- Cahyadi, M. N., Rahayu, R. W., Heki, K., & Nakashima, Y. (2020). Harmonic ionospheric oscillation by the 2010 eruption of the Merapi volcano, Indonesia, and the relevance of its amplitude to the mass eruption rate. *Journal of Volcanology and Geothermal Research*, 405, 107047. <https://doi.org/10.1016/j.jvolgeores.2020.107047>
- Chapman, S. (1931). The absorption and dissociative or ionizing effect of monochromatic radiation in an atmosphere on a rotating earth Part II. Grazing incidence. *Proceedings of the Physical Society*, 43(5), 483–501. <https://doi.org/10.1088/0959-5309/43/5/302>
- Chen, P., Xiong, M., Wang, R., Yao, Y., Tang, F., Chen, H., & Qiu, L. (2023). On the ionospheric disturbances in New Zealand and Australia following the eruption of the Hunga Tonga–Hunga Ha’apai volcano on 15 January 2022. *Space Weather*, 21(4), e2022SW003294. <https://doi.org/10.1029/2022sw003294>
- Coster, A., Williams, J., Weatherwax, A., Rideout, W., & Herne, D. (2013). Accuracy of GPS total electron content: GPS receiver bias temperature dependence. *Radio Science*, 48(2), 190–196. <https://doi.org/10.1002/rds.20011>
- Duncombe, J. (2022). The surprising reach of Tonga’s giant atmospheric waves. 774 Eos: AGU Science News.103.
- Eble, M. C., & Gonzalez, F. I. (1991). Deep-ocean bottom pressure measurements in the northeast Pacific. *Journal of Atmospheric and Oceanic Technology*, 8(2), 221–233. [https://doi.org/10.1175/1520-0426\(1991\)008<0221:dobpmi>2.0.co;2](https://doi.org/10.1175/1520-0426(1991)008<0221:dobpmi>2.0.co;2)
- Fuller-Rowell, T. J., Millward, G. H., Richmond, A. D., & Codrescu, M. V. (2002). Storm-time changes in the upper atmosphere at low latitudes. *Journal of Atmospheric and Solar-Terrestrial Physics*, 64(12–14), 1383–1391. [https://doi.org/10.1016/s1364-6826\(02\)00101-3](https://doi.org/10.1016/s1364-6826(02)00101-3)
- Ghent, J. N., & Crowell, B. W. (2022). Spectral characteristics of ionospheric disturbances over the southwestern Pacific from the 15 January 2022 Tonga eruption and tsunami. *Geophysical Research Letters*, 49(20), e2022GL100145. <https://doi.org/10.1029/2022gl100145>
- Gusman, A. R., & Roger, J. (2022). *Hunga Tonga–Hunga Ha’apai volcano-induced sea level oscillations and tsunami simulations*. GNS Science webpage. <https://doi.org/10.21420/DYKJ-RK41>
- Gusman, A. R., Roger, J., Noble, C., Wang, X., Power, W., & Burbidge, D. (2022). The 2022 Hunga Tonga–Hunga Ha’apai volcano air-wave generated tsunami. *Pure and Applied Geophysics*, 179(10), 3511–3525. <https://doi.org/10.1007/s00024-022-03154-1>
- Harding, B. J., Wu, Y. J. J., Alken, P., Yamazaki, Y., Triplett, C. C., Immel, T. J., et al. (2022). Impacts of the January 2022 Tonga volcanic eruption on the ionospheric dynamo: ICON-MIGHTI and Swarm observations of extreme neutral winds and currents. *Geophysical Research Letters*, 49(9), e2022GL098577. <https://doi.org/10.1029/2022gl098577>
- He, L., & Heki, K. (2018). Three-dimensional tomography of ionospheric anomalies immediately before the 2015 Illapel earthquake, Central Chile. *Journal of Geophysical Research: Space Physics*, 123(5), 4015–4025. <https://doi.org/10.1029/2017ja024871>
- Heidarzadeh, M., Gusman, A. R., Ishibe, T., Sabeti, R., & Šepić, J. (2022). Estimating the eruption-induced water displacement source of the 15 January 2022 Tonga volcanic tsunami from tsunami spectra and numerical modelling. *Ocean Engineering*, 261, 112165. <https://doi.org/10.1016/j.oceaneng.2022.112165>
- Heki, K. (2011). Ionospheric electron enhancement preceding the 2011 Tohoku-Oki earthquake. *Geophysical Research Letters*, 38(17), L17312. <https://doi.org/10.1029/2011gl047908>
- Heki, K. (2022). Ionospheric signatures of repeated passages of atmospheric waves by the 2022 Jan. 15 Hunga Tonga–Hunga Ha’apai eruption detected by QZSS-TEC observations in Japan. *Earth Planets and Space*, 74(1), 1–12. <https://doi.org/10.1186/s40623-022-01674-7>
- Heki, K., & Cahyadi, M. N. (2012). Precursory changes in ionosphere immediately before mega-thrust earthquakes. In *AGU Fall Meeting Abstracts* (Vol. 2012).NH43C-04.
- Heki, K., & Ping, J. (2005). Directivity and apparent velocity of the coseismic ionospheric disturbances observed with a dense GPS array. *Earth and Planetary Science Letters*, 236(3–4), 845–855. <https://doi.org/10.1016/j.epsl.2005.06.010>
- Hu, G., Li, L., Ren, Z., & Zhang, K. (2023). The characteristics of the 2022 Tonga volcanic tsunami in the Pacific Ocean. *Natural Hazards and Earth System Sciences*, 23(2), 675–691. <https://doi.org/10.5194/nhess-23-675-2023>
- Huang, C. S. (2020). Systematical analyses of global ionospheric disturbance current systems caused by multiple processes: Penetration electric fields, solar wind pressure impulses, magnetospheric substorms, and ULF waves. *Journal of Geophysical Research: Space Physics*, 125(9), e2020JA027942. <https://doi.org/10.1029/2020ja027942>
- Jenan, R., Dammalage, T. L., & Panda, S. K. (2022). Ionospheric TEC response to severe geomagnetic storm and annular solar eclipse through GNSS based TEC observations and assessment of IRI-2016 model and global ionosphere maps over Sri Lankan equatorial and low latitude region. *Astrophysics and Space Science*, 367(2), 24. <https://doi.org/10.1007/s10509-022-04051-8>
- Jin, S. G., Jin, R., & Kutoglu, H. (2017). Positive and negative ionospheric responses to the March 2015 geomagnetic storm from BDS observations. *Journal of Geodesy*, 91(6), 613–626. <https://doi.org/10.1007/s00190-016-0988-4>
- Jin, S. G., Occhipinti, G., & Jin, R. (2015). GNSS ionospheric seismology: Recent observation evidences and characteristics. *Earth-Science Reviews*, 147, 54–64. <https://doi.org/10.1016/j.earscirev.2015.05.003>

- Jin, S. G., & Su, K. (2019). Co-seismic displacement and waveforms of the 2018 Alaska earthquake from high-rate GPS PPP velocity estimation. *Journal of Geodesy*, 93(9), 1559–1569. <https://doi.org/10.1007/s00190-019-01269-3>
- Jin, S. G., Wang, Q., & Dardanelli, G. (2022). A review on multi-GNSS for Earth observation and emerging applications. *Remote Sensing*, 14(16), 3930. <https://doi.org/10.3390/rs14163930>
- Kakinami, Y., Kamogawa, M., Tanioka, Y., Watanabe, S., Gusman, A. R., Liu, J. Y., & Mogi, T. (2012). Tsunamigenic ionospheric hole. *Geophysical Research Letters*, 39(13), L00G27. <https://doi.org/10.1029/2011gl050159>
- Kamogawa, M., Orihara, Y., Tsurudome, C., Tomida, Y., Kanaya, T., Ikeda, D., et al. (2016). A possible space-based tsunami early warning system using observations of the tsunami ionospheric hole. *Scientific Reports*, 6(1), 37989. <https://doi.org/10.1038/srep37989>
- Kanamori, H., Mori, J., & Harkrider, D. G. (1994). Excitation of atmospheric oscillations by volcanic eruptions. *Journal of Geophysical Research*, 99(B11), 21947–21961. <https://doi.org/10.1029/94jb01475>
- Le, G., Liu, G., Yizengaw, E., & Englert, C. R. (2022). Intense equatorial electrojet and counter electrojet caused by the 15 January 2022 Tonga volcanic eruption: Space- and ground-based observations. *Geophysical Research Letters*, 49(11), e2022GL099002. <https://doi.org/10.1029/2022gl099002>
- Li, W., Zhu, H., Feng, J., Wu, X., Tang, J., Zhang, Z., & Chen, J. (2023). Asymmetric ionospheric fluctuations over the circum-Pacific regions following the January 2022 Tonga volcanic eruption. *Space Weather*, 21(8), e2022SW003213. <https://doi.org/10.1029/2022sw003213>
- Liu, J. Y., Chen, C. H., Lin, C. H., Tsai, H. F., Chen, C. H., & Kamogawa, M. (2011). Ionospheric disturbances triggered by the 11 March 2011 M9.0 Tohoku earthquake. *Journal of Geophysical Research*, 116(A6), A06319. <https://doi.org/10.1029/2011ja016761>
- Liu, J. Y., Tsai, Y. B., Ma, K. F., Chen, Y. I., Tsai, H. F., Lin, C. H., et al. (2006). Ionospheric GPS total electron content (TEC) disturbances triggered by the 26 December 2004 Indian Ocean tsunami. *Journal of Geophysical Research: Space Physics*, 111(A5), L02103. <https://doi.org/10.1029/2005ja011200>
- Meinig, C., Stalin, S. E., Nakamura, A. I., & Milburn, H. B. (2005). *Real-time deep-ocean tsunami measuring, monitoring, and reporting system: The NOAA DART II description and disclosure* (pp. 1–15). NOAA, Pacific Marine Environmental Laboratory (PMEL).
- Muafiry, I. N., & Heki, K. (2020). 3-D tomography of the ionospheric anomalies immediately before and after the 2011 Tohoku-oki (Mw9.0) earthquake. *Journal of Geophysical Research: Space Physics*, 125(10), e2020JA027993. <https://doi.org/10.1029/2020ja027993>
- Muafiry, I. N., Heki, K., & Maeda, J. (2018). 3D tomography of midlatitude sporadic-E in Japan from GNSS-TEC data. *Earth Planets and Space*, 70(1), 1–12. <https://doi.org/10.1186/s40623-018-0815-7>
- Muafiry, I. N., Meilano, I., Heki, K., Wijaya, D. D., & Nugraha, K. A. (2022). Ionospheric disturbances after the 2022 Hunga Tonga–Hunga Ha’apai eruption above Indonesia from GNSS-TEC observations. *Atmosphere*, 13(10), 1615. <https://doi.org/10.3390/atmos13101615>
- Munaibari, E., Rolland, L. M., Sladen, A., & Delouis, B. (2023). Anatomy of the tsunami and Lamb waves-induced ionospheric signatures generated by the 2022 Hunga Tonga volcanic eruption. *Authorea Preprints*, 180(5), 1751–1764. <https://doi.org/10.1007/s00024-023-03271-5>
- Muslim, B., Cahyadi, M. N., Sunardi, B., & Kumalasari, C. J. (2020). The simulation study of GNSS signal reflection in monitoring sea levels and tsunami. *Science of Tsunami Hazards*, 39(4), 192–209.
- Nakashima, Y., Heki, K., Takeo, A., Cahyadi, M. N., & Aditiya, A. (2014). Ionospheric disturbances by volcanic eruptions by GNSS-TEC: Comparison between Vulcanian and Plinian eruptions. In *AGU Fall Meeting Abstracts* (Vol. 2014). NH33C-05.
- Nakashima, Y., Heki, K., Takeo, A., Cahyadi, M. N., Aditiya, A., & Yoshizawa, K. (2016). Atmospheric resonant oscillations by the 2014 eruption of the Kelud volcano, Indonesia, observed with the ionospheric total electron contents and seismic signals. *Earth and Planetary Science Letters*, 434, 112–116. <https://doi.org/10.1016/j.epsl.2015.11.029>
- Ogawa, T., Kumagai, H., & Sinno, K. (1982). Ionospheric disturbances over Japan due to the 18 May 1980 eruption of Mount St. Helens. *Journal of Atmospheric and Terrestrial Physics*, 44(10), 863–868. [https://doi.org/10.1016/0021-9169\(82\)90039-3](https://doi.org/10.1016/0021-9169(82)90039-3)
- Omira, R., Ramalho, R. S., Kim, J., González, P. J., Kadri, U., Miranda, J. M., et al. (2022). Global Tonga tsunami explained by a fast-moving atmospheric source. *Nature*, 609(7928), 1–2. <https://doi.org/10.1038/s41586-022-04926-4>
- Qiu, L., Zuo, X., Yu, T., Sun, Y., & Qi, Y. (2019). Comparison of global morphologies of vertical ion convergence and sporadic E occurrence rate. *Advances in Space Research*, 63(11), 3606–3611. <https://doi.org/10.1016/j.asr.2019.02.024>
- Rakoto, V., Lognonné, P., & Rolland, L. (2017). Tsunami modeling with solid Earth–ocean–atmosphere coupled normal modes. *Geophysical Journal International*, 211(2), 1119–1138. <https://doi.org/10.1093/gji/ggx322>
- Richmond, A. D., & Matsushita, S. (1975). Thermospheric response to a magnetic substorm. *Journal of Geophysical Research*, 80(19), 2839–2850. <https://doi.org/10.1029/ja080i019p02839>
- Rolland, L. M., Occhipinti, G., Lognonné, P., & Loevenbruck, A. (2010). Ionospheric gravity waves detected offshore Hawaii after tsunamis. *Geophysical Research Letters*, 37(17), L17101. <https://doi.org/10.1029/2010gl044479>
- Saito, S. (2022). Ionospheric disturbances observed over Japan following the eruption of Hunga Tonga–Hunga Ha’apai on 15 January 2022. *Earth Planets and Space*, 74(1), 1–9. <https://doi.org/10.1186/s40623-022-01619-0>
- Savastano, G., Komjathy, A., Verkhoglyadova, O., Mazzoni, A., Crespi, M., Wei, Y., & Mannucci, A. J. (2017). Real-time detection of tsunami ionospheric disturbances with a stand-alone GNSS receiver: A preliminary feasibility demonstration. *Scientific Reports*, 7(1), 46607. <https://doi.org/10.1038/srep46607>
- Scherliess, L., & Fejer, B. G. (1997). Storm time dependence of equatorial disturbance dynamo zonal electric fields. *Journal of Geophysical Research*, 102(A11), 24037–24046. <https://doi.org/10.1029/97ja02165>
- Sharma, G., Mohanty, S., & Kannaujya, S. (2017). Ionospheric TEC modelling for earthquakes precursors from GNSS data. *Quaternary International*, 462, 65–74. <https://doi.org/10.1016/j.quaint.2017.05.007>
- Shinagawa, H., & Miyoshi, Y. (2023). Simulation study of atmosphere-ionosphere variations driven by the eruption of Hunga Tonga–Hunga Ha’apai on 15 January 2022.
- Shinbori, A., Otsuka, Y., Sori, T., Nishioka, M., Perwitasari, S., Tsuda, T., & Nishitani, N. (2022). Electromagnetic conjugacy of ionospheric disturbances after the 2022 Hunga Tonga–Hunga Ha’apai volcanic eruption as seen in GNSS-TEC and SuperDARN Hokkaido pair of radars observations. *Earth Planets and Space*, 74(1), 1–17. <https://doi.org/10.1186/s40623-022-01665-8>
- Shults, K., Astafyeva, E., & Adourian, S. (2016). Ionospheric detection and localization of volcano eruptions on the example of the April 2015 Calbuco events. *Journal of Geophysical Research: Space Physics*, 121(10), 10–303. <https://doi.org/10.1002/2016ja023382>
- Sori, T., Shinbori, A., Otsuka, Y., Tsugawa, T., & Nishioka, M. (2021). The occurrence feature of plasma bubbles in the equatorial to midlatitude ionosphere during geomagnetic storms using long-term GNSS-TEC data. *Journal of Geophysical Research: Space Physics*, 126(5), e2020JA029010. <https://doi.org/10.1029/2020ja029010>
- Takenaka, H., Sakashita, T., Higuchi, A., & Nakajima, T. (2020). Development of geolocation correction for geostationary satellite observation by phase only correlation method using visible channel. *Remote Sensing*, 12(15), 2472. <https://doi.org/10.3390/rs12152472>

- Taylor, G. I. (1932). The resonance theory of semidiurnal atmospheric oscillations. *Roy. Meteorol. Soc.*, 4(9), 41–52.
- Themens, D. R., Watson, C., Žagar, N., Vasylyevych, S., Elvidge, S., McCaffrey, A., et al. (2022). Global propagation of ionospheric disturbances associated with the 2022 Tonga volcanic eruption. *Geophysical Research Letters*, 49(7), e2022GL098158. <https://doi.org/10.1029/2022gl098158>
- Vergoz, J., Hupe, P., Listowski, C., Le Pichon, A., Garcés, M. A., Marchetti, E., et al. (2022). IMS observations of infrasound and acoustic-gravity waves produced by the January 2022 volcanic eruption of Hunga, Tonga: A global analysis. *Earth and Planetary Science Letters*, 591, 117639. <https://doi.org/10.1016/j.epsl.2022.117639>
- Wang, H., Xia, H., & Zhang, K. (2022). Variations in the equatorial ionospheric F region current during the 2022 Tonga volcanic eruption. *Remote Sensing*, 14(24), 6241. <https://doi.org/10.3390/rs14246241>
- Weathernews (2022). Sudden changes in atmospheric pressure due to shock-waves from Tonga volcanic eruption observed. global.weathernews.com/news/16551.
- Witze, A. (2022). Why the Tongan eruption will go down in the history of volcanology. *Nature*, 602(7897), 376–378. <https://doi.org/10.1038/d41586-022-00394-y>
- Yamamoto, Y., Ichii, K., Higuchi, A., & Takenaka, H. (2020). Geolocation accuracy assessment of Himawari-8/AHI imagery for application to terrestrial monitoring. *Remote Sensing*, 12(9), 1372. <https://doi.org/10.3390/rs12091372>
- Zhang, K., Wang, H., Zhong, Y., Xia, H., & Qian, C. (2022). The temporal evolution of F-region equatorial ionization anomaly owing to the 2022 Tonga volcanic eruption. *Remote Sensing*, 14(22), 5714. <https://doi.org/10.3390/rs14225714>
- Zhang, K. D., Wang, H., & Yamazaki, Y. (2022). Effects of subauroral polarization streams on the equatorial electrojet during the geomagnetic storm on 1 June, 2013: 2. The temporal variations. *Journal of Geophysical Research: Space Physics*, 127(2), e2021JA030180. <https://doi.org/10.1029/2021JA030180>
- Zhang, K. D., Wang, H., Yamazaki, Y., & Xiong, C. (2021). Effects of subauroral polarization streams on the equatorial electrojet during the geomagnetic storm on June 1, 2013. *Journal of Geophysical Research: Space Physics*, 126(10), e2021JA029681. <https://doi.org/10.1029/2021JA029681>
- Zhang, S. R., Vierinen, J., Aa, E., Goncharenko, L. P., Erickson, P. J., Rideout, W., et al. (2022). 2022 Tonga volcanic eruption induced global propagation of ionospheric disturbances via Lamb waves.
- Zhong, Y. F., Wang, H., Luehr, H., Zhang, K. D., Xia, H., Qian, C. Y., et al. (2023). Local time variations of the ionospheric F layer radial current in response to enhanced solar wind input. *Journal of Geophysical Research: Space Physics*, 128(12), e2023JA031709. <https://doi.org/10.1029/2023JA031709>